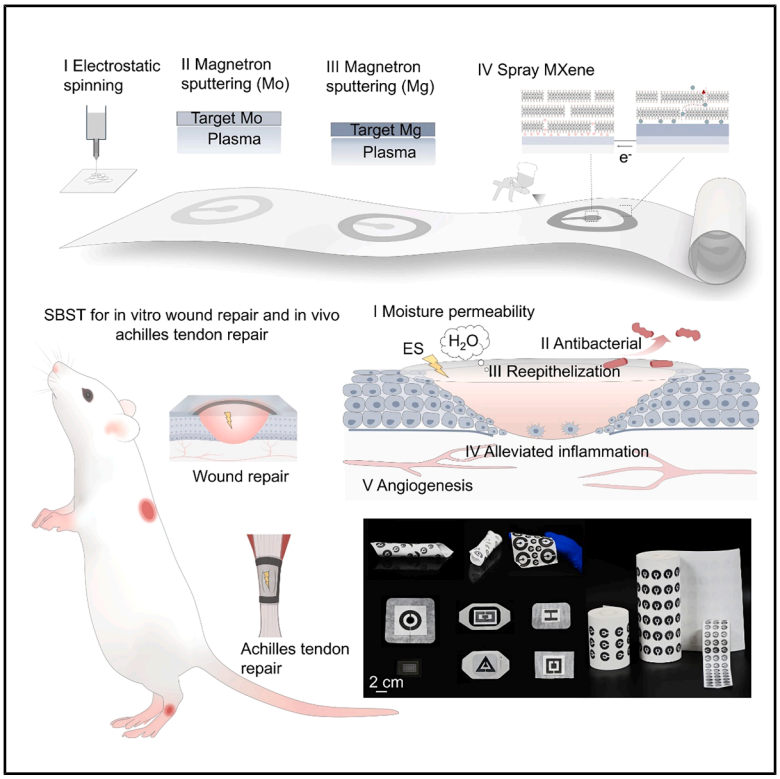
Cell Biomaterials

Article

Tissue-fluid-driven symbiotic electronic textile accelerates and guides tissue self-healing

Graphical abstract



Highlights

- Tissue-fluid-driven, self-powered bioelectronics
- MXene enhances the stability of the soft electronic textile
- Fully bioresorbable design enables the device to safely disappear after therapy
- Electronic textile accelerates and guides tissue self-healing

Authors

Engui Wang, Lingling Xu, Lin Luo, ..., Jiaping Zhang, Zhou Li, Han Ouyang

Correspondence

xulingling@ucas.ac.cn (L.X.), japzhang@aliyun.com (J.Z.), li_zhou@tsinghua.edu.cn (Z.L.), ouyanghan@ucas.ac.cn (H.O.)

In brief

Electrical stimulation can enhance tissue repair, but conventional devices rely on external power and rigid, nondegradable components, limiting clinical applicability. A tissue-fluid-driven, self-powered, fully bioresorbable symbiotic electronic textile autonomously delivers sustained electrical cues. By integrating MXene-regulated ion transport with biodegradable metals, this soft, breathable device accelerates and guides skin and tendon healing in mice and diabetic pigs.

Wang et al., 2026, Cell Biomaterials 2, 100375
October 20, 2026 © 2026 The Author(s). Published by Elsevier Inc.
https://doi.org/10.1016/j.celbio.2026.100375

CellPress

Please cite this article in press as: Wang et al., Tissue-fluid-driven symbiotic electronic textile accelerates and guides tissue self-healing, Cell Biomaterials (2026), https://doi.org/10.1016/j.celbio.2026.100375

Cell Biomaterials

CellPress
OPEN ACCESS

Article

Tissue-fluid-driven symbiotic electronic textile accelerates and guides tissue self-healing

Engui Wang,[1] Lingling Xu,[1,2,*] Lin Luo,[1] Yongfang Ren,[1] Yichang Quan,[1] Tian Le,[1] Jiangtao Xue,[1] Chang Zhu,[1] Jing Huang,[1] Xi Cui,[2,3] Dongjie Jiang,[4] Bojing Shi,[5] Hongqing Feng,[1] Jiaping Zhang,[6,*] Zhou Li,[2,3,*] and Han Ouyang[1,7,*]

[1]School of Nanoscience and Engineering, School of Chemical Sciences, University of Chinese Academy of Sciences, Beijing 100049, China
[2]Vita Tech Innovation Center, Tsinghua Changgung Hospital, School of Clinical Medicine, Tsinghua University, Beijing 100084, China
[3]School of Biomedical Engineering, Tsinghua Medicine, Tsinghua University, Beijing 100084, China
[4]Department of Advanced Manufacturing and Robotics, College of Engineering, Peking University, Beijing 100871, China
[5]Key Laboratory for Biomechanics and Mechanobiology of the Chinese Education Ministry, Beijing Advanced Innovation Centre for Biomedical Engineering, School of Biological Science and Medical Engineering, Beihang University, Beijing 100191, China
[6]Department of Plastic Surgery, State Key Laboratory of Trauma, Burns and Combined Injury, Southwest Hospital, Third Military Medical University (Army Medical University), Chongqing 400038, China
[7]Lead contact
*Correspondence: xulingling@ucas.ac.cn (L.X.), japzhang@aliyun.com (J.Z.), li_zhou@tsinghua.edu.cn (Z.L.), ouyanghan@ucas.ac.cn (H.O.)
https://doi.org/10.1016/j.celbio.2026.100375

THE BIGGER PICTURE Electrical stimulation has emerged as a powerful therapeutic strategy for promoting tissue repair, yet its clinical impact is still limited by bulky power supplies, rigid device architectures, and nondegradable components that compromise patient comfort, safety, and compliance. This work introduces a tissue-fluid-driven, self-powered, and fully bioresorbable symbiotic electronic textile that integrates active bioelectronic therapy into a soft, breathable, and conformable textile platform. By harvesting endogenous tissue fluid to generate sustained electrical stimulation and employing MXene-regulated ion transport with biodegradable metals, the system operates autonomously without external power sources, leads, or device retrieval. Importantly, the device gradually degrades after completing its therapeutic function, thereby eliminating the need for secondary surgical removal. The demonstrated efficacy in accelerating and guiding skin and tendon repair, including validation in diabetic large-animal models, underscores its strong translational potential. This study introduces a new class of symbiotic bioelectronics, self-driven by tissue fluids to generate electrical stimulation that accelerates wound healing and safely degrades afterward. This innovation paves the way for scalable, biodegradable, and patient-friendly bioelectronic therapies in regenerative medicine.

SUMMARY

Electrical stimulation is a powerful strategy for promoting tissue self-healing, yet conventional systems are limited by reliance on external power sources, rigid components, and low conformability to dynamic tissue surfaces. Here, we report a tissue-fluid-driven, self-powered, fully bioresorbable symbiotic electronic textile (SBST) that integrates controllable electrical stimulation into a thin, breathable, and fully degradable textile while preserving essential wound-care functionality. By incorporating Magnesium (Mg)/Molybdenum (Mo) nanoelectrodes with an MXene ion-transport layer (80 ± 2.3 μm thick, 70 ± 3.1 mg), SBST avoids direct electrochemical contact with tissue and provides stable electrical output. *In vivo* studies demonstrate that SBST significantly enhances Achilles tendon regeneration in rats, accelerates skin wound healing, and exhibits effective antibacterial activity in mice and diabetic pigs. Its textile-compatible, lead-free design highlights SBST as a promising platform for next-generation, clinically translatable electrical stimulation therapies.

INTRODUCTION

Tissue damage can lead to infection, inflammatory responses, and long-term tissue remodeling abnormalities that always impact local functional recovery and even possibly result in organ dysfunction.[1–6] Although living tissues possess intrinsic regenerative capacity, the process is often slow or incomplete under pathological conditions. Electrical stimulation can accelerate and guide tissue self-healing with precise and reliable treatment results and few side effects and has achieved remarkable clinical

This is an open access article under the CC BY-NC license (http://creativecommons.org/licenses/by-nc/4.0/).

Please cite this article in press as: Wang et al., Tissue-fluid-driven symbiotic electronic textile accelerates and guides tissue self-healing, Cell Biomaterials (2026), https://doi.org/10.1016/j.celbio.2026.100375

advances in chronic wound healing, nerve regeneration, and bone fusion.[7–21] Its therapeutic mechanisms mainly involve modulating cell membrane potential, promoting cell proliferation and migration, enhancing collagen synthesis, and improving local blood circulation, thereby accelerating the tissue repair process.[9,22] However, additional external power sources, leads, rigid packages, device retention, etc., severely limit patient benefits and compliance. Disruptive morphology design and power supply are keys to overcoming these limitations.[23–26]

In terms of power supply, the main methods include external power sources, wireless power transmission, and triboelectric and piezoelectric energy harvesting.[15,27–37] However, each of these approaches has its limitations. External power sources provide adjustable and stable parameters but rely on bulky cables, which severely limit their applicability. Wireless transmission devices require external power sources such as radio frequency, light, or ultrasound, restricting patient mobility and necessitating precisely designed stimulation systems that rely on expensive and cumbersome equipment. Triboelectric and piezoelectric methods have the advantage of being self-powered but suffer from instability and spatial limitations. Therefore, developing a lightweight, flexible, leadless, and self-powered electrical stimulation device is of great significance for advancing the field of tissue damage care.

In recent years, galvanic cell-based self-powered electrical stimulation systems have attracted increasing attention for wound healing and nerve repair, as they can continuously generate direct currents *in situ* without relying on external energy input.[9,11,38,39] However, existing systems still face key limitations, including unstable output from uncontrolled electrochemical reactions, short operational lifetimes due to rapid electrode degradation, and low conformability to dynamic tissue surfaces. In many cases, electrochemical reactions occur in direct contact with tissue fluids, leading to output fluctuations and potential tissue irritation. As a result, few systems simultaneously achieve stable long-term operation, conformal and leadless configuration, and full bioresorbability. From a device morphology perspective, medical textiles are widely used in clinical wound care due to their breathability, softness, comfort, and ability to maintain a favorable healing microenvironment.[40–45] These properties make textile platforms attractive for electrical stimulation therapies. However, integrating controllable, self-powered electrical stimulation into a thin, breathable, and fully bioresorbable textile while preserving its essential wound-care functions remains a significant and unmet challenge.

Here, we introduced a self-powered bioresorbable symbiotic electronic textile (SBST) that addresses these challenges. The SBST consisted of a breathable electrospun polycaprolactone (PCL) substrate, an Mg/Mo metal-functionalized electronic layer, and an MXene ion-transport layer and has a thickness of 80 ± 2.3 μm and a mass of 70 ± 3.1 mg. Distinct from conventional galvanic systems, SBST avoided direct electrochemical reactions at the wound interface by incorporating an MXene ion-transport layer, enabling stable and well-controlled self-powered electrical stimulation. Benefiting from its textile architecture, SBST conformed intimately to irregular tissue surfaces, maintained breathability and moisture permeability, and supported routine wound care. *In vivo* studies demonstrate that SBST effectively accelerates and guides tissue repair in mouse skin and rat Achilles tendon models, with further validation in a diabetic pig wound model. Compared with representative electrical stimulation wound devices (Table S1), SBST uniquely integrated self-powered operation, stable output, softness, and full bioresorbability within a single textile platform. These features clearly distinguished SBST in terms of stimulation stability, clinical practicality, and translational potential, providing a new strategy for next-generation leadless and power-free electrical stimulation therapies.

RESULTS AND DISCUSSION

Design philosophy of SBST

SBST integrates electrical stimulation therapy with medical textiles to promote tissue self-healing and prevent infection. It consists of a biodegradable PCL fiber substrate, Mg/Mo-functionalized nanoelectrodes electronic layer, and an MXene ion-transport layer (Figures 1A, 1B, and S1). Mg and Mo were selected because both are biodegradable metals with biocompatible and non-toxic degradation products. Mg provides a highly negative electrochemical potential for stable galvanic output, while Mo degrades more slowly, ensuring a durable and sustained cathodic interface during operation. MXene was selected for its lamellar nanochannels that enable efficient ion transport and stable regulation of Mg electrochemical reactions while providing high conductivity at ultrathin thickness, good physiological stability, and controllable biodegradability (Tables S2 and S3). The electrospun PCL fibers provide excellent breathability and flexibility, while mask-assisted sputtering enables patterned Mg/Mo nanoelectrodes to generate a radial electric field (EF) aligned with the endogenous bioelectric cues. The concentric-circle electrode design ensures a uniform EF matching the tissue's centripetal healing direction and provides a large, stable Mg/Mo interface for reliable self-powered stimulation. This alignment promotes directional cell migration and proliferation and optimizes the local repair environment.

Spray-coated MXene self-assembles to form uniform two-dimensional (2D) nanochannels on the Mg electrode, regulating water molecule and ion transport and moisture permeability. These nanochannels guide tissue exudate to activate the Mg oxidation reaction, providing continuous electrical stimulation (Figure 1C), which promotes tissue repair through antimicrobial properties, facilitates re-epithelialization, reduces inflammation, and accelerates angiogenesis. Meanwhile, the confined Mg ion transport slows down electrode degradation, thereby extending device lifespan.

SBST is lightweight (70 ± 3.1 mg), ultrathin (80 ± 2.3 μm), and highly flexible and can be readily customized into various geometries to conform to soft tissue environments. Its fabrication process is not only seamlessly compatible with existing medical textile systems but also demonstrates feasibility and stability for large-scale production (Figure 1D), thereby laying a solid foundation for clinical translation and industrialization. In addition, SBST exhibits reliable *in vitro* degradability (Figure S2). Overall, SBST outperforms previously reported biodegradable electrical stimulation devices for tissue repair in terms of flexibility, power output, degradability, and cost-effectiveness (Figure 1E; Table S4).

Please cite this article in press as: Wang et al., Tissue-fluid-driven symbiotic electronic textile accelerates and guides tissue self-healing, Cell Biomaterials (2026), https://doi.org/10.1016/j.celbio.2026.100375

CellPress
OPEN ACCESS

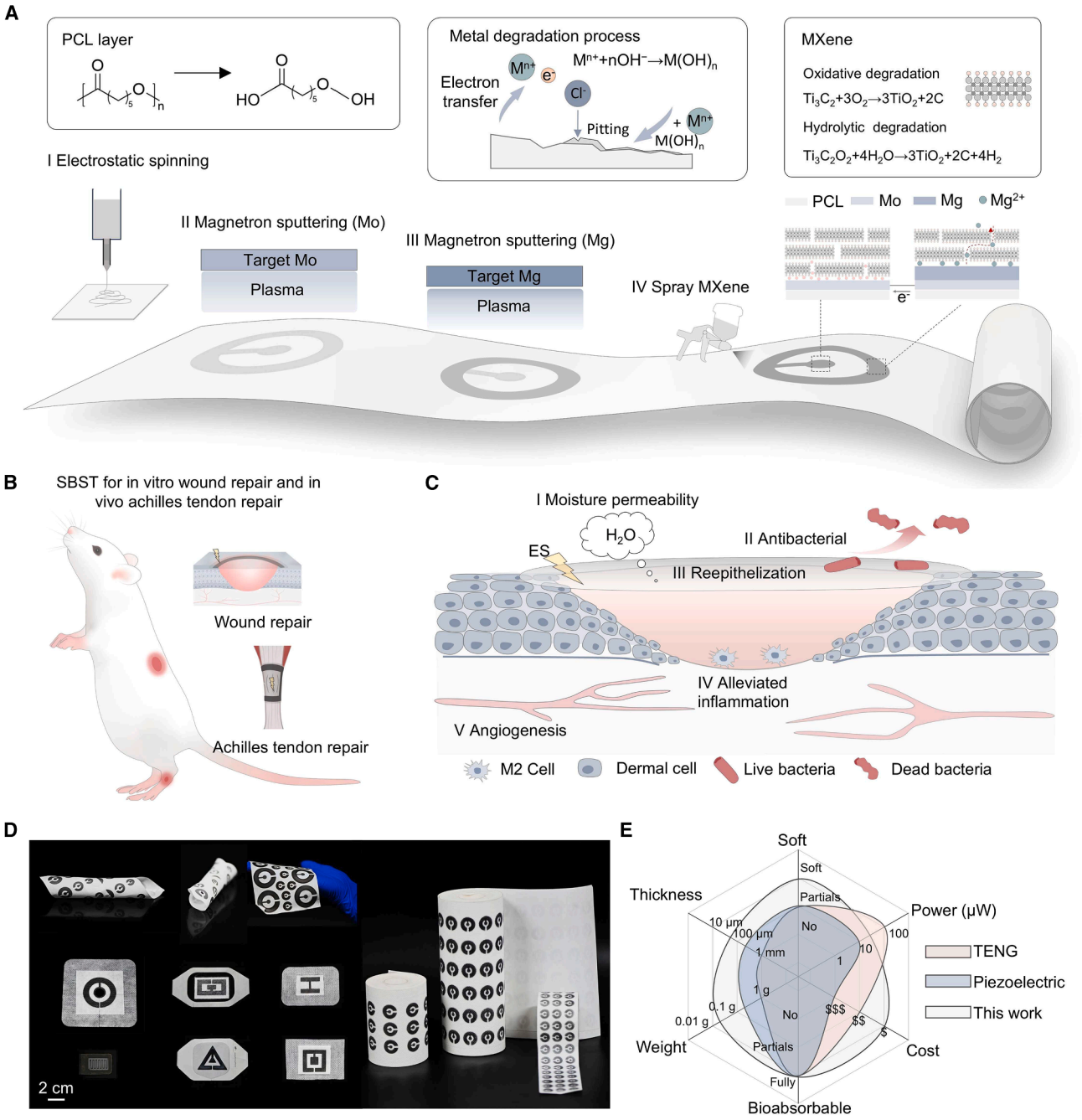


Figure 1. Materials, design, and working principle of SBST

(A) Preparation process diagram of SBST.
(B) SBST for tissue repair.
(C) Mechanism of SBST accelerating tissue repair.
(D) Physical image of SBST.
(E) Comparison of SBST-related indicators with previously reported works.

Material and electrical characterization of SBST

An MXene 2D nanosheet ion confinement layer was self-assembled on the surface of the magnesium nanoelectrode layer to limit ion transport, extend device lifetime, and regulate device impedance to be comparable to that of biological tissues (Figure 2A). The capillary-driven water transport within the MXene channels ensures stable current generation while limiting excessive reaction (Figure 2B). Energy dispersive X-ray spectroscopy (EDS) mapping confirmed the elemental distribution before and after MXene assembly (Figures 2C and S3). The

Please cite this article in press as: Wang et al., Tissue-fluid-driven symbiotic electronic textile accelerates and guides tissue self-healing, Cell Biomaterials (2026), https://doi.org/10.1016/j.celbio.2026.100375

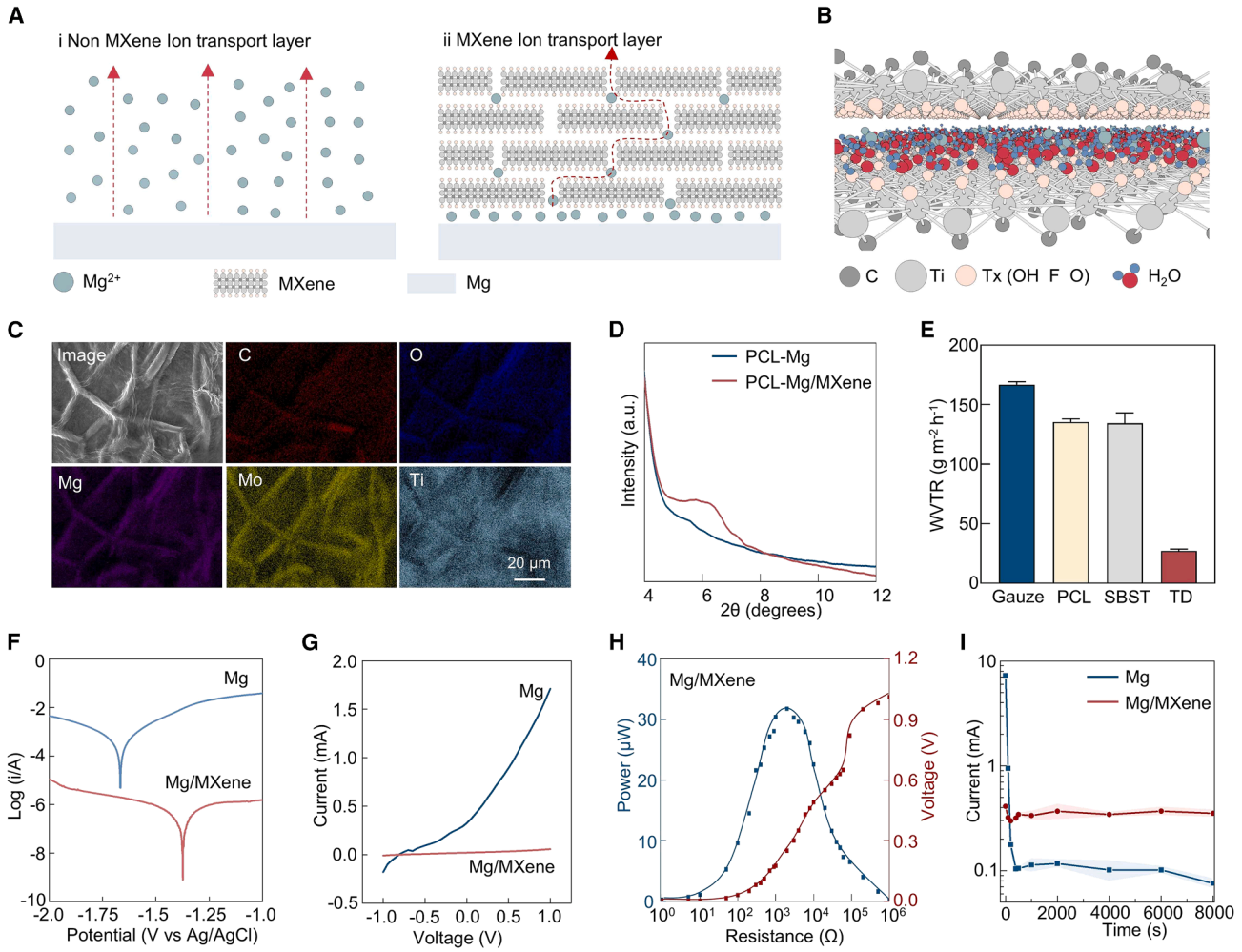


Figure 2. The materials and electrochemical characterizations of SBST

(A) Schematic illustration of Mg ion transport with or without MXene nanofluid, diffusion behavior of Mg ions (Ai), ion transport at the Mg metal surface with MXene nanofluid (Aii).
(B) Schematic illustration of Mg ion diffusion in MXene nanofluid.
(C) Elemental distribution of SBST.
(D) XRD patterns of Mg and Mg/MXene.
(E) WVTRs of different materials (n = 3).
(F) Tafel curves of Mg and Mg/MXene.
(G) I-V curves of Mg and Mg/MXene.
(H) Voltage and power at different resistances.
(I) Current output variations of Mg and Mg/MXene.
In (E), data are presented as mean ± SD.

X-ray diffraction (XRD) patterns showed a characteristic diffraction peak at 6.3°—this indicates that the MXene layer has a highly ordered stacking arrangement. Using Bragg's law, the d-spacing (interlayer spacing) of the MXene layer was calculated to be 1.43 nm (Figure 2D). Furthermore, the strong adhesion of MXene to the SBST surface was verified through mechanical bending tests (Figure S4).

The SBST exhibits excellent breathability with a water vapor transmission rate (WVTR) of up to 130 gm^{-2} h^{-1} (Figures 2E and S5), which facilitates gas and nutrient exchange for tissue healing. The stress-strain curve indicated mechanical flexibility comparable to that of soft tissue (900 kPa–6 MPa), ensuring comfortable tissue conformity (Figures S6 and S7). At the same time, SBST has excellent hydrophilicity, which ensures its close attachment to tissues (Figure S8).

Electrochemical testing was used to further analyze the robustness and stability of SBTS as an electrical stimulation device. Tafel curves showed that MXene coating reduced corrosion potential (1.66 to 1.37 V) and had a 1,000-fold lower corrosion current (Figure 2F). I-V curves and impedance analysis revealed that the presence of the MXene nanolayer regulated charge transport, leading to an increased internal impedance (Figure 2G). The

Please cite this article in press as: Wang et al., Tissue-fluid-driven symbiotic electronic textile accelerates and guides tissue self-healing, Cell Biomaterials (2026), https://doi.org/10.1016/j.celbio.2026.100375

CellPress
OPEN ACCESS

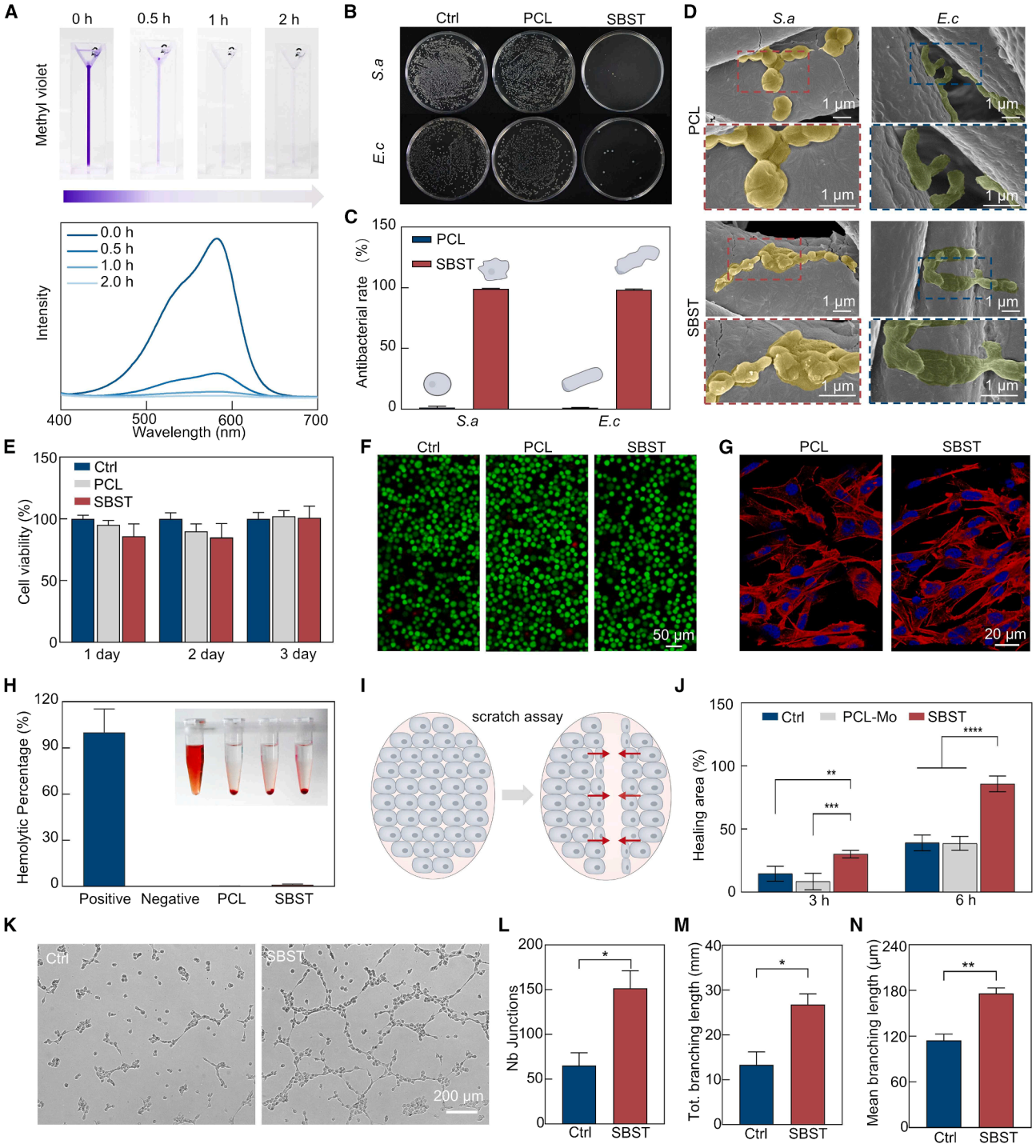


Figure 3. SBST antibacterial performance and cell experiments

(A) SBST degrading methyl violet.

(B) The photos of CFU plating of *E. coli* and *S. aureus* after being treated with PCL and SBST.

(C) Bacteria killing ratio of PCL and SBST (n = 3).

(D) SEM images of *S. aureus* (yellow) and *E. coli* (green) on PCL and SBST.

(E) Cell viability percentage (n = 6).

(F) Cell live/dead staining.

(G) Cell skeleton staining on the surface of different materials.

(legend continued on next page)

Please cite this article in press as: Wang et al., Tissue-fluid-driven symbiotic electronic textile accelerates and guides tissue self-healing, Cell Biomaterials (2026), https://doi.org/10.1016/j.celbio.2026.100375

SBTS can deliver efficient output of no less than 20 μW across the entire range of biological tissue impedance loads (200–10,000 ohms) (Figures 2H and S9). The Mg/MXene maintained a steady current of 350 μA, while pure Mg rapidly decayed from 7 mA to 100 μA (Figure 2I). These findings highlight the critical role of the MXene ion-transport layer in protecting the Mg electrode, reducing its corrosion rate, and significantly extending its operational lifespan. These results demonstrate that MXene self-assembled ion confinement transport layers are responsible for the improved stability and robustness of SBTS.

Furthermore, electrical testing was performed under various biochemical environments, and the results show that, due to the presence of the MXene ion-transport layer, the output of SBST remains largely unchanged, confirming that SBST can provide stable electrical stimulation in wound environments (Figures S10–S12).

Antibacterial properties and biocompatibility

Bacterial infection is a major factor delaying tissue healing, highlighting the critical need for antibacterial properties to support effective tissue regeneration. Based on the principle of primary battery operation, SBST generates electrical energy through redox reactions at the electrode interface that induce electron transfer, consequently leading to the production of reactive oxygen species (ROS) in localized regions. These ROS are hypothesized to disrupt bacterial cell membranes and thereby exert antibacterial effects. To test this hypothesis, we investigated whether SBST's antibacterial activity is mediated by free radical production. Using methyl violet (a dye that undergoes oxidative degradation in the presence of active oxygen species), the changes in its absorption peak were monitored by spectrophotometry as an indirect measure of ROS generation. Degradation experiments demonstrated that SBST induced the degradation and decolorization of methyl violet, achieving a 99% degradation rate within 2 h, thereby indirectly confirming the generation of ROS (Figure 3A).

In subsequent *in vitro* antibacterial tests, the antibacterial performance of SBST against *E. coli* and *S. aureus* was evaluated by co-culture experiments. As shown in Figure 3B, SBST exhibited remarkable antibacterial rates of 98% and 99% against *E. coli* and *S. aureus*, respectively (Figure 3C), while PCL fibers showed negligible antibacterial activity. Scanning electron microscope (SEM) images further revealed that bacteria on PCL fibers maintained normal morphology, while those on SBST exhibited severe membrane damage and structural collapse (Figure 3D). These results demonstrate the excellent antibacterial capability of SBST. Importantly, *in vivo* antibacterial experiments further confirmed that SBST effectively inhibited bacterial growth at the wound site, demonstrating its antibacterial performance under physiological conditions (Figure S13).

In addition, the biocompatibility of SBST was systematically evaluated. Cell Counting Kit-8 (CCK-8) assays showed a cell viability of ~100% within 3 days of culture (Figure 3E), consistent with live/dead staining results (Figure 3F). Cell skeleton staining further confirmed excellent cell adhesion and spreading on SBST (Figure 3G). Moreover, SBST exhibited a low hemolysis rate of 1.1%, considerably lower than the 5% threshold defined by International Organization for Standardization standards (Figure 3H). These results confirm the favorable biosafety and non-cytotoxicity of SBST for tissue defect-contact applications.

Effect of electrical stimulation on cell migration and proliferation

To evaluate the effect of SBST on cell migration, an *in vitro* scratch tissue healing assay was performed using human keratinocyte cells, which play a crucial role in wound healing. The results demonstrated that SBST significantly promoted cell migration (Figure 3I). After 6 h of stimulation, the wound closure percentages in the Ctrl, PCL, and SBST groups were 39.1%, 38.5%, and 85.8%, respectively, with the SBST group showing a 2.2-fold larger healed area than the Ctrl group ($p < 0.0001$) (Figures 3J and S14). Furthermore, an atrigel tube formation assay was conducted to evaluate the effect of SBST on the angiogenic capacity of human umbilical vein endothelial cells (HUVECs). After 4 h of culture, more tubular structures were observed in the SBST group (Figure 3K). Quantitative analysis showed that the number of junctions, total branch length, and average branching length increased by 2.5-fold (65 vs. 151.5, $p = 0.012$), 2-fold (13.36 vs. 26.78 mm, $p = 0.0112$), and 1.7-fold (114.42 vs. 176.14 μm, $p = 0.0013$), respectively (Figures 3L–3N). These results suggest that electrical stimulation may regulate cell migration and tube formation by polarizing the cell membrane potential and activating the phosphatidylinositol 3-kinase (PI3K)/Protein Kinase B (Akt) and extracellular signal-regulated kinase (ERK) signaling pathways, thereby effectively accelerating the angiogenic process of endothelial cells and enhancing the complexity of vascular networks.

In vivo electrical testing

Following skin injury, a stable endogenous EF develops within the injured tissue, critically influencing cell migration and promoting tissue repair and remodeling. In this study, we designed a concentric-structured SBST dressing based on the galvanic cell principle, consisting of central and peripheral electrodes, to enhance the endogenous EF (Figures 4A and 4B). To investigate the influence of different electrode configurations on tissue repair, we fabricated two types of electrode arrangements: SBST-S with magnesium in the outer ring and SBST-M with magnesium in the center (Figure S15).

(H) Hemolysis ratio results of positive control, negative control, PCL, and SBST ($n = 4$).
(I) Schematic diagram of cell scratch experiment.
(J) Statistical graph of cell healing area ($n = 4$).
(K) Cell morphology images under different treatments.
(L) Statistical graph of the number of cell connections ($n = 4$).
(M) Statistical graph of total branch length ($n = 4$).
(N) Statistical graph of average branch length ($n = 4$).
In (C), (E), (H), (J), and (L)–(N), data are presented as mean ± SD. In (J), statistical significance was determined by the one-way ANOVA, $^{*}p < 0.05$, $^{**}p < 0.01$, $^{***}p < 0.001$, $^{****}p < 0.0001$. In (L)–(N), statistical significance was determined by the unpaired *t* test, $^{*}p < 0.05$, $^{**}p < 0.01$.

Please cite this article in press as: Wang et al., Tissue-fluid-driven symbiotic electronic textile accelerates and guides tissue self-healing, Cell Biomaterials (2026), https://doi.org/10.1016/j.celbio.2026.100375

CellPress
OPEN ACCESS

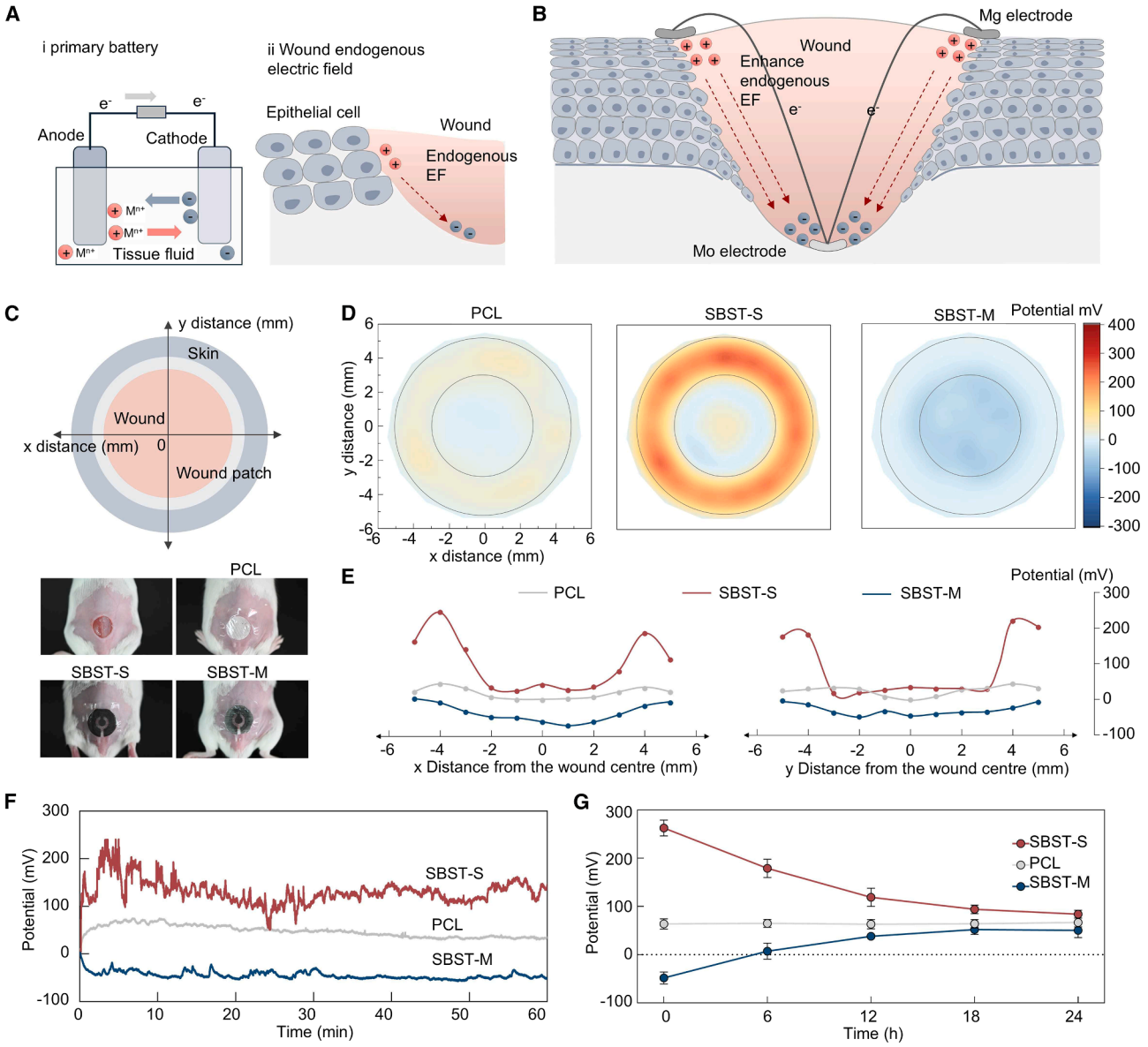


Figure 4. SBST in electrochemical characterization

(A) Schematic diagram of the original battery and the endogenous EF in the wound.
(B) Schematic diagram of SBST acting on the tissue wound.
(C) Schematic diagram of SBST attached to the tissue.
(D) Wound potential distribution of different SBST.
(E) Potential distribution along the *x-y* axis direction.
(F) Change of wound potential within 60 min.
(G) Change of wound potential at different time points.

As shown in Figure 4C, we established a coordinate system with the wound center as the origin and measured the effect of each dressing on the potential distribution across the wound region. The corresponding wound potentials are presented in Figure 4D. Compared with the PCL control group, the SBST-S group exhibited a more uniform and significantly enhanced potential at the wound edge, whereas the SBST-M group showed a lower potential at the wound edge relative to the center. The EF strength in the PCL group was approximately 60 mV/mm, consistent with the typical level of endogenous EFs in normal wounds. In the SBST-S group, the EF strength was increased to approximately 240 mV/mm, attributed to the oxidation of magnesium at the outer ring, which generates Mg^{2+} ions and electrons. The electrons are transferred via an external circuit to the central cathode, thereby enhancing the local wound EF. By contrast, the electrode polarity in the SBST-M configuration

Please cite this article in press as: Wang et al., Tissue-fluid-driven symbiotic electronic textile accelerates and guides tissue self-healing, Cell Biomaterials (2026), https://doi.org/10.1016/j.celbio.2026.100375

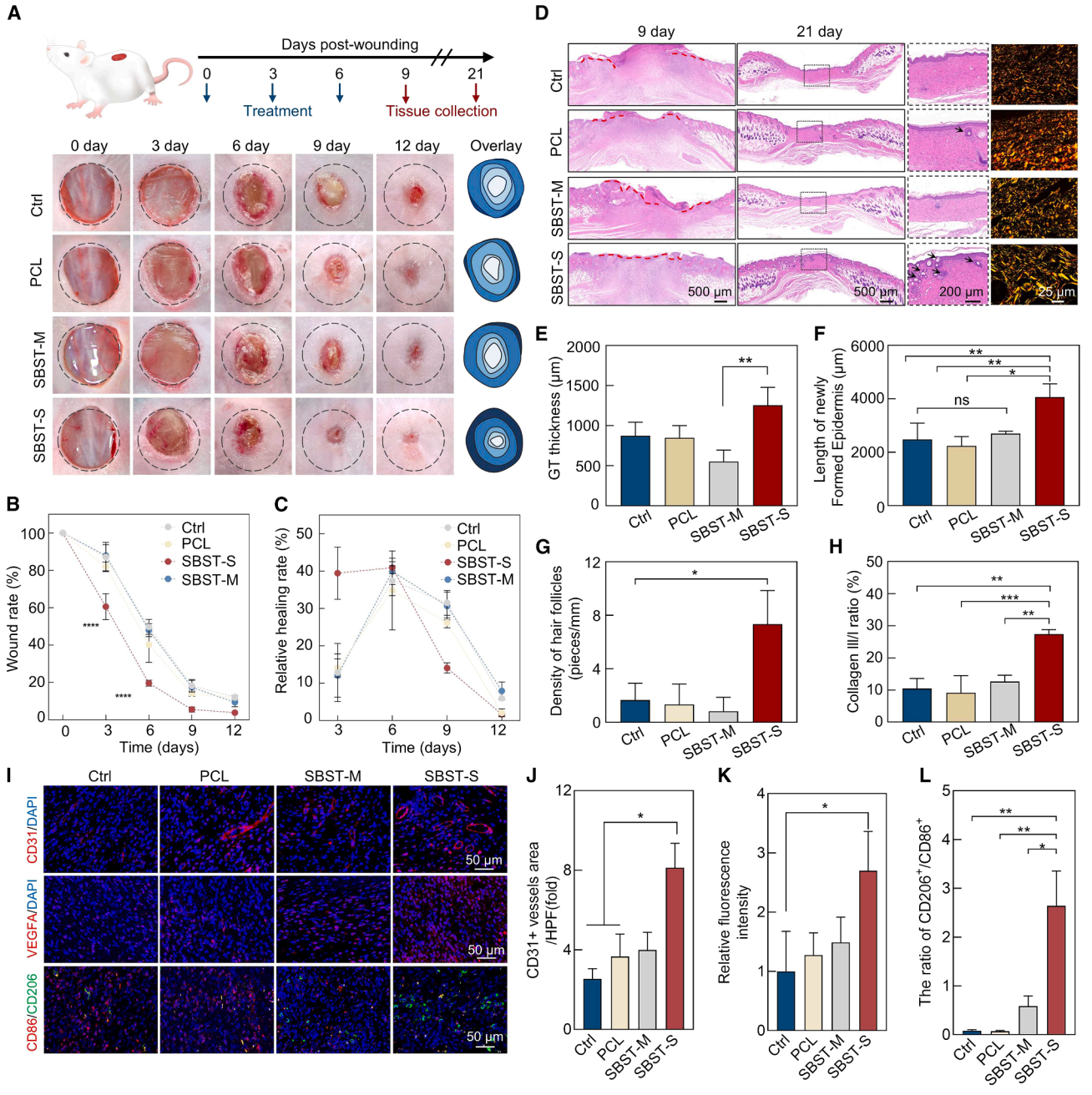


Figure 5. Evaluation of SBST in a full-thickness skin defect mouse model

(A) Representative images of wound healing in mice from different experimental groups at different time points.
(B) Statistical analysis of wound areas in each group at different time points (n = 3).
(C) Statistical analysis of relative wound-healing rates in each group at different time points (n = 3).
(D) H&E staining of wound tissue at days 9 and 21 post-injury and Sirius Red staining at day 21.
(E) Statistical analysis of granulation tissue at day 9 (n = 3).
(F) Statistical analysis of new epithelial length at day 9 (n = 3).
(G) Statistical analysis of hair follicle density at day 21 (n = 3).
(H) Statistical analysis of collagen ratio at day 21 (n = 3).
(I) Immunofluorescence staining of tissue sections at day 9.
(J) Statistical analysis of $CD31^+$ blood vessel area/high power field at day 9 (n = 3).

(legend continued on next page)

Please cite this article in press as: Wang et al., Tissue-fluid-driven symbiotic electronic textile accelerates and guides tissue self-healing, Cell Biomaterials (2026), https://doi.org/10.1016/j.celbio.2026.100375

was reversed, resulting in an inverted EF of approximately −60 mV/mm across the wound region (Figures 4E and S16).

We continuously monitored the wound potential in mice for 60 min, and the results indicated that the SBST dressing could maintain a relatively stable wound potential during this period (Figure 4F). Furthermore, time-course measurements revealed that the EF in both SBST-S and SBST-M groups gradually returned to baseline levels after 24 h, likely due to the complete oxidation of magnesium and the consequent decline in the galvanic output (Figure 4G). In addition, temperature monitoring confirmed that SBST did not induce any detectable changes in wound temperature during operation, indicating that the electrical stimulation process does not introduce thermal disturbance to the wound environment (Figure S17). A skin wound model based on three-dimensional (3D) finite element analysis (FEA) further demonstrated the electrical stimulation effect of SBST on the wound (Figure S18). Benefiting from the MXene ion-transport layer, the electrical stimulation generated by SBST remains stable and well confined within a biologically safe and effective therapeutic range.[22,23] The lamellar nanochannels of MXene increase interfacial impedance and regulate ion flux, thereby smoothing the EF and preventing excessive current output while ensuring sustained, therapeutically relevant stimulation.

Evaluation of SBST accelerated skin tissue self-healing in mouse model

To further evaluate the *in vivo* therapeutic efficacy of SBST dressings in promoting tissue regeneration, a full-thickness skin wound model (1 cm diameter) was established on Kunming (KM) mice. Wounds were treated with Tegaderm (Ctrl), PCL, SBST-M (Mg at the center), and SBST-S (Mg at the edge), respectively, and all wounds were covered with Tegaderm film to ensure consistent fixation and minimize skin contraction, which could otherwise affect the healing process. Wound images were recorded every 3 days, and tissues were collected on days 9 and 21 for histological analysis.

Among all groups, SBST-S exhibited the most pronounced acceleration in skin tissue (Figure 5A). Quantitative analysis revealed that on day 3, the injured tissue area of the SBST-S group (60%) was significantly smaller than that of the Ctrl (87%), PCL (82%), and SBST-M (88%) groups ($p < 0.0001$). On day 6, the injured tissue area in SBST-S decreased to 19.69%, markedly lower than that in Ctrl (49.75%), PCL (40.22%), and SBST-M (48.04%) groups ($p < 0.0001$) (Figure 5B). Notably, SBST-S accelerated healing already in the early stages of tissue injury, with significant improvement observed on both days 3 and 6 (Figures 5C and S19). By day 12, injured tissue in the SBST-S group was almost completely closed, while injured tissue in other groups remained incompletely healed. Histological analysis using hematoxylin and eosin (H&E) staining was performed to evaluate granulation tissue formation and re-epithelialization. On day 9, the SBST-S group showed the thickest granulation tissue and the longest neo-epidermis (Figures 5D–5F), indicating an accelerated healing process. Notably, newly formed hair follicles were observed in the SBST-S group on postoperative day 21 (Figure 5G), indicating an improved quality of skin regeneration. Sirius Red staining further demonstrated that the collagen III/I ratio in the SBST-S group was higher than that in other groups and closer to normal skin (Figure 5H), indicating better tissue elasticity without excessive scar formation. Masson's trichrome staining (Figure S20) showed that collagen fibers in the SBST-S group were more densely and uniformly arranged, whereas those in the Ctrl, PCL, and SBST-M groups appeared disorganized and loosely packed, implying that SBST-S facilitated more orderly tissue remodeling. Moreover, SBST-S significantly promoted angiogenesis. Immunofluorescence staining of CD31 showed a markedly increased $CD31^+$ vessel area in the SBST-S group compared with the other groups (Figures 5I, 5J, and S21), confirming the pro-angiogenic effect of SBST-S, which facilitates nutrient and oxygen supply to the wound site.

Notably, no significant differences were observed in wound-healing rate or tissue regeneration outcomes among the control groups (Ctrl, PCL, and SBST-M), as validated by multiple parameters, including wound area, healing rate, tissue morphology, and vascularization at various time points. These results suggest that PCL, as an inert material, exerted minimal influence on the healing process. The distinct healing outcomes of SBST-S and SBST-M arise from their opposite EF orientations. SBST-S aligns with the endogenous centripetal healing direction and promotes organized tissue repair, whereas SBST-M generates a reversed field that disrupts natural bioelectric cues. Although this opposite polarity may exert a suppressive influence on healing, SBST-M did not show impaired outcomes compared with the other control groups.

No significant changes in body weight were observed throughout the wound-healing experiments (Figure S22). Histological analysis of major organs revealed no pathological abnormalities (Figure S23), and blood biochemistry and complete blood count analyses showed no detectable deviations from normal ranges (Figure S24). In addition, subcutaneous implantation of SBST in mice further confirmed its favorable *in vivo* biocompatibility and biosafety, demonstrating that the material does not induce adverse local or systemic responses (Figure S25; Table S5).

Transcriptome analysis

To investigate the potential mechanisms by which SBST promotes tissue regeneration, we performed mRNA sequencing analysis of wound tissues collected on day 6 post-injury from the control group (C), SBST-M group (M), and SBST-S group (S). Using a threshold of fold change > 1.5 and p value < 0.05, significant differences in gene expression were observed among the three groups (Figure 6A). Upset plot analysis revealed distinct gene expression patterns between groups. Pairwise comparisons (Figures 6B and 6C) identified differentially expressed genes (DEGs), which were subsequently subjected to Kyoto Encyclopedia of Genes and Genomes (KEGG) enrichment analysis

(K) Semi-quantitative results of VEGFA relative fluorescence intensity at day 9 ($n = 3$).
(L) Statistical analysis of CD206+/CD86+ macrophage ratio at day 9 ($n = 3$).
In (B), (E)–(H), and (J)–(L), data are presented as mean ± SD. In (B), (E)–(H), and (J)–(L), statistical significance was determined by the one-way ANOVA, $^*p < 0.05$, $^{**}p < 0.01$, $^{***}p < 0.001$, $^{****}p < 0.0001$.

CellPress
OPEN ACCESS

Cell Biomaterials
Article

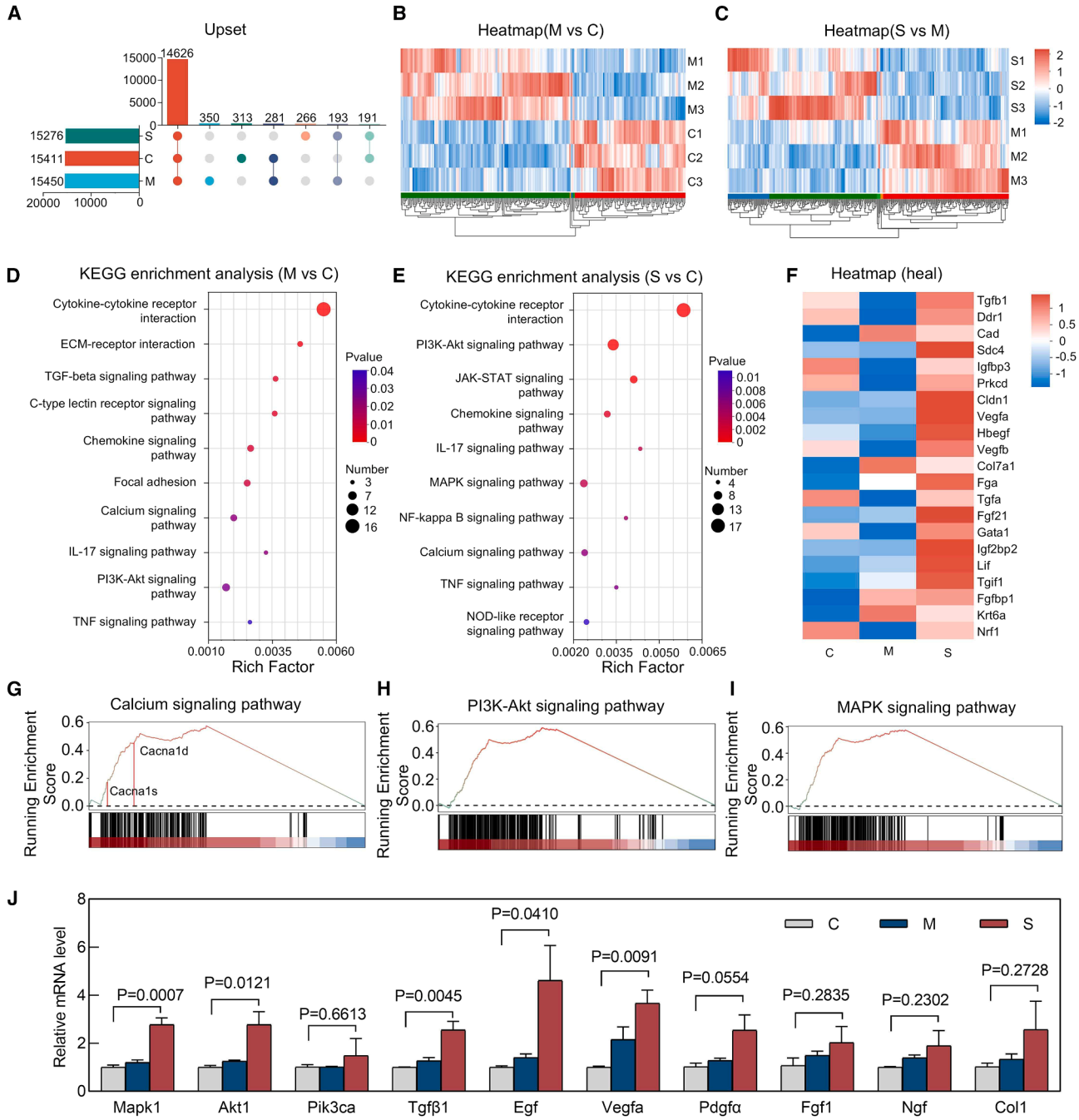


Figure 6. Exploration of gene expression patterns and functional enrichment analysis

(A) Upset plot of shared and unique genes between groups.
(B and C) Heatmap of gene expression differences between different groups.
(D and E) Enrichment analysis of differential genes between different groups (n = 3).
(F) Heatmap of healing-related genes.
(G–I) GSEA analysis of related signaling pathways for GSEA-related genes.
(J) Quantitative analysis of mRNA relative gene expression levels (n = 3).
In (J), data are presented as mean ± SD. In (J), statistical significance was determined by the one-way ANOVA.

Please cite this article in press as: Wang et al., Tissue-fluid-driven symbiotic electronic textile accelerates and guides tissue self-healing, Cell Biomaterials (2026), https://doi.org/10.1016/j.celbio.2026.100375

(Figures 6D and 6E). The results indicated that multiple signaling pathways potentially involved in SBST-mediated tissue healing were significantly enriched, including vascular endothelial growth factor (VEGF), tumor necrosis factor (TNF), nuclear factor κB (NF-κB), interleukin (IL)-17, extracellular matrix (ECM)-receptor interaction, and adenosine 5'-monophosphate -activated protein kinase (AMPK) signaling pathways.

Gene Ontology (GO) enrichment analysis revealed that compared with the control group, the SBST-M group showed activation of biological processes primarily associated with tissue structural organization, cellular regulation, and responses to external stimuli, suggesting a regulatory role in wound healing (Figure S26). By contrast, the SBST-S group exhibited broader biological regulatory effects, including enhanced ECM remodeling, developmental regulation, response to external stimuli, and cell proliferation and differentiation, indicating a more comprehensive impact on wound repair. Heatmap (Figure 6F) analysis demonstrated that the SBST-S group significantly upregulated a panel of genes closely associated with tissue regeneration, including those involved in growth factor signaling, ECM reconstruction (Col7a1, Fga, Sdc4, and Ddr1), angiogenesis (Vegfa and Vegfb), and cellular adhesion, proliferation, and migration (Tgfb1, Hbegf, Tgfa, Fgf21, Lif, Fgfbp1, Krt6a, and Cad). Gene set enrichment analysis (GSEA) (Figures 6G and 6I) further confirmed enrichment of the PI3K-Akt, mitogen-activated protein kinase (MAPK), and calcium signaling pathways. The coordinated upregulation of these genes suggests that SBST-S effectively modulates the wound microenvironment and activates multiple regeneration-related pathways in a synergistic manner.

To validate the transcriptomic findings, we further performed quantitative real-time PCR (real-time qPCR) to assess the relative mRNA expression of key genes in wound tissues. Results showed that the PI3K-Akt signaling pathway and its associated genes (Mapk1 and Akt1) were significantly upregulated in the SBST-S group. Genes related to tissue regeneration and angiogenesis (Tgfβ1, Egf, and Vegfa) were also significantly increased, while Pdgfα, Fgf1, Ngf, and Col1 exhibited an upward trend without reaching statistical significance (Figure 6J).

Collectively, these findings suggest that SBST-S promotes wound healing by activating multiple signaling pathways related to angiogenesis, cell proliferation, and tissue regeneration, thereby effectively enhancing the wound repair process.

Evaluation of SBST accelerated and guided tendon tissue self-healing *in vivo*

To further evaluate the tissue repair capacity of SBST, an Achilles tendon injury model was established in Sprague-Dawley (SD) rats (Figure 7A), and the animals were randomly divided into three groups: Ctrl, PCL, and SBST. In this study, to better adapt the scaffold for tendon repair, the PCL scaffold was fabricated with aligned fibers, providing topographical cues that guided cellular migration and alignment along the fiber direction (Figure S27). This structural feature facilitated collagen deposition and tissue remodeling, partially mimicking the native architecture of the Achilles tendon and thus serving as a physical template for tendon regeneration. Building on this structural guidance, the SBST group further incorporated a stable primary battery-driven electrical stimulation, thereby establishing a dual-regulation strategy that synergistically combined physical and electrical cues.

In vivo electrical performance testing (Figure S28) confirmed that SBST could generate a stable electric output, whereas the PCL group exhibited no measurable signal. Notably, in the Achilles tendon repair model, SBST maintained an output of approximately 60 mV after 3 weeks of implantation, which is sufficient to meet the electrical stimulation requirements for tissue repair (Figure S29). Gait analysis (Figures 7B and S30) demonstrated that the SBST group achieved the most pronounced recovery in motor function, with improvements in stride length, symmetry, and stability, approaching normal levels by week 4. The Achilles tendon functional index (Figure 7C) further supported that the SBST group exhibited superior functional recovery throughout the healing period. The PCL group also showed a moderate enhancement in repair capacity, possibly attributable to the highly aligned fiber architecture that promoted cell orientation and tenogenic differentiation.

At week 4, gross morphological examination of the repaired tendons (Figure 7D) revealed that the SBST group presented a more native-like tendon appearance. Histological analysis (Figure 7E) confirmed that, compared with the PCL group, SBST treatment resulted in a well-organized tendon-like structure with parallel collagen fibers, dense ECM, and spindle-shaped tenoblasts and tenocytes—features closely resembling native tendon. By contrast, the Ctrl and PCL groups displayed more rounded cells, inflammatory infiltration, and a less dense ECM, indicating limited regenerative capacity. Masson's trichrome staining (Figure 7E, bottom) further revealed a higher proportion of mature collagen in the SBST group.

Quantitative analysis of the collagen volume fraction (Figure 7F) demonstrated that the SBST group exhibited significantly higher collagen content compared with both the Ctrl group and the PCL group (33.92% and 41.09%, respectively; $p < 0.001$). Additionally, orientation-mapped Masson images (Figure 7G) highlighted the superior alignment of collagen fibers in the SBST group, consistent with orientation analysis results (Figure 7H), where SBST-treated tendons showed the highest degree of fiber alignment and order.

Taken together, these findings suggest that SBST effectively promotes Achilles tendon regeneration by providing continuous electrical stimulation that enhances cell migration, proliferation, and collagen deposition. Based on *in vivo* observations and known material degradation behaviors, SBST is expected to fully biodegrade within approximately 6–12 months, primarily governed by the slow degradation of PCL.

Evaluation of SBST accelerated and guided difficult-to-heal skin tissue self-healing in the diabetic porcine model

To further validate the therapeutic efficacy and translational potential of SBST in skin tissue healing, a porcine full-thickness wound model was established, which closely resembles human skin in both structure and healing dynamics, providing a clinically relevant evaluation. Specifically, a diabetes model was established in Bama mini pigs via streptozotocin (STZ) induction, with continuous monitoring of blood glucose levels and body weight throughout the experiment. Twelve full-thickness circular wounds (1.5 cm in

Please cite this article in press as: Wang et al., Tissue-fluid-driven symbiotic electronic textile accelerates and guides tissue self-healing, Cell Biomaterials (2026), https://doi.org/10.1016/j.celbio.2026.100375

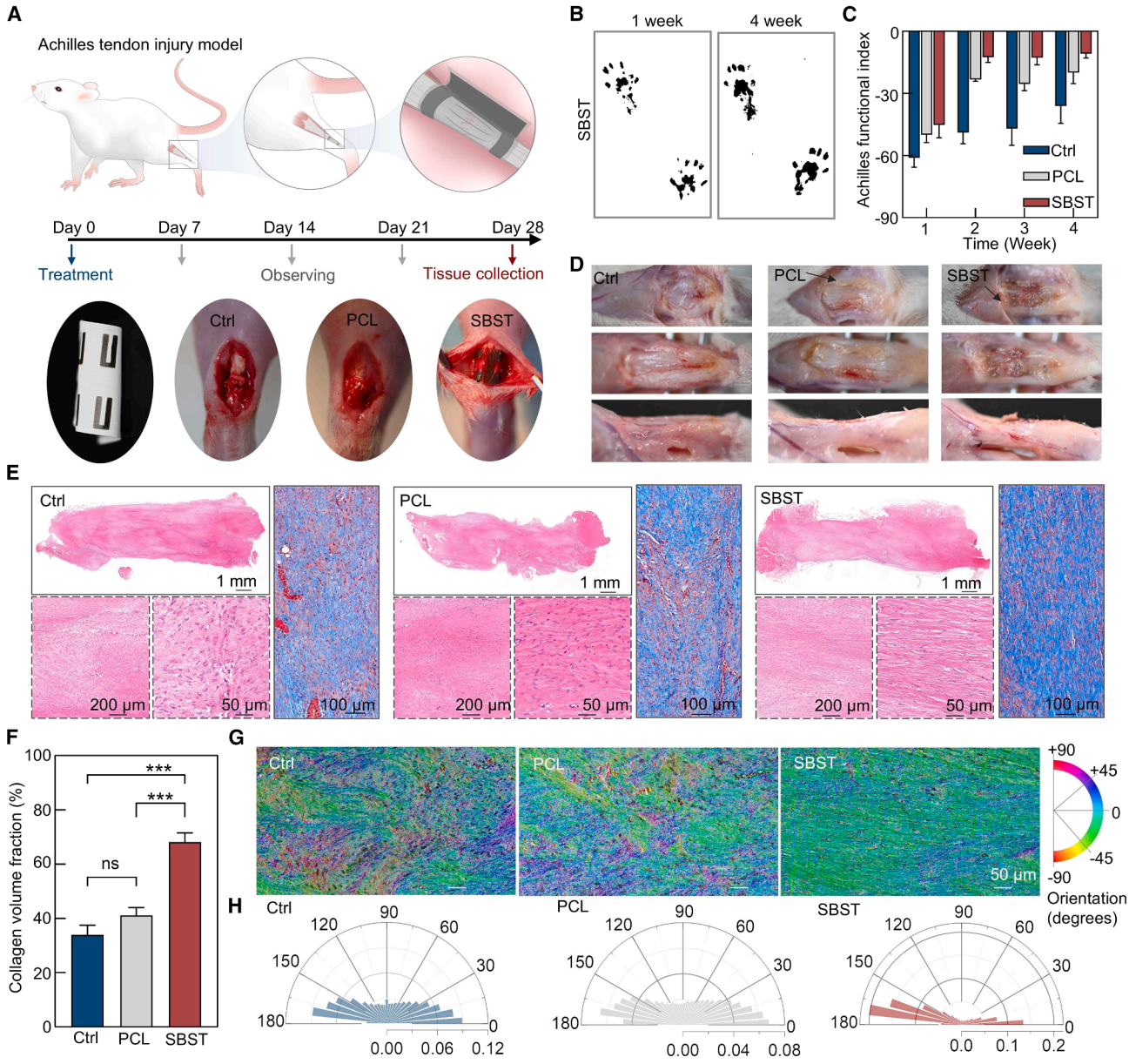


Figure 7. SBST is used in the rat Achilles tendon rupture model

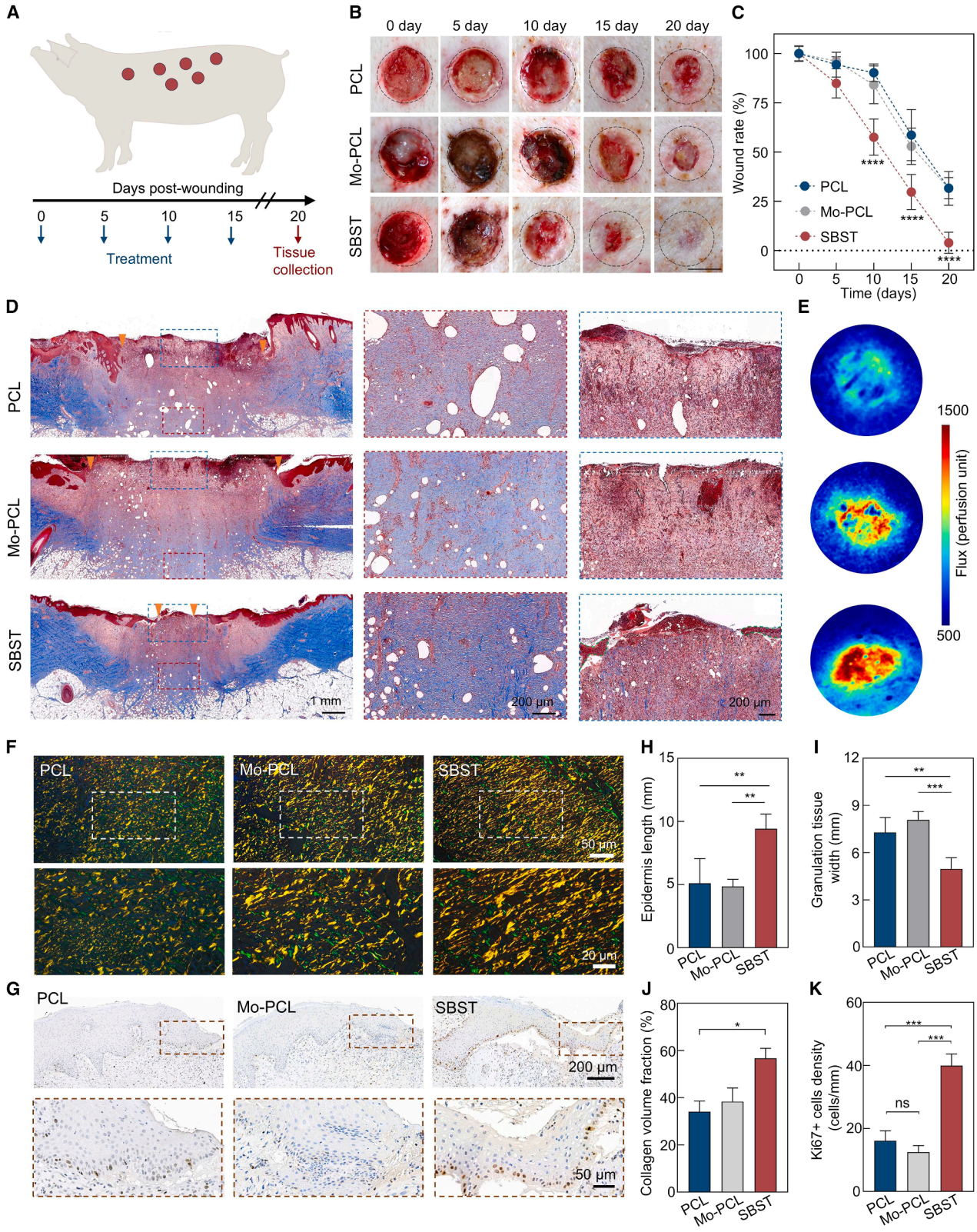
(A) Schematic diagram of SBST used in rat Achilles tendon repair.
(B) Gait images of the SBST experimental group at different time points.
(C) Achilles tendon function index of different experimental groups (n = 3).
(D) Photographs of Achilles tendons in different experimental groups after 4 weeks of treatment.
(E) H&E and Masson staining of different experimental groups.
(F) Statistical analysis of collagen volume fraction in different experimental groups (n = 4).
(G) The orientation-mapped Masson images of the Achilles tendon in the Ctrl, PCL, and SBST groups.
(H) Corresponding orientation analysis data.
In (F), data are presented as mean ± SD. In (F), statistical significance was determined by the one-way ANOVA. *$p < 0.05$, **$p < 0.01$, ***$p < 0.001$, ****$p < 0.0001$.

diameter) were created on the dorsal skin (Figure 8A) and were alternately treated with PCL (control), Mo-PCL, and SBST dressings to minimize potential bias caused by wound location.

Local potential measurements (Figure S31) demonstrated that SBST dressing significantly enhanced the endogenous EF strength at the wound site, and this effect was sustained throughout the healing process. By contrast, the PCL and Mo-PCL groups exhibited negligible changes in local potential, suggesting a lack of effective regulation of the wound electric microenvironment. Wound closure was monitored and quantified over

Please cite this article in press as: Wang et al., Tissue-fluid-driven symbiotic electronic textile accelerates and guides tissue self-healing, Cell Biomaterials (2026), https://doi.org/10.1016/j.celbio.2026.100375

CellPress
OPEN ACCESS



(legend on next page)

Please cite this article in press as: Wang et al., Tissue-fluid-driven symbiotic electronic textile accelerates and guides tissue self-healing, Cell Biomaterials (2026), https://doi.org/10.1016/j.celbio.2026.100375

time (Figures 8B and 8C), showing that the SBST group consistently achieved higher healing rates at all time points. By postoperative day 10, the average wound-healing rate in the SBST group reached 42.48%, significantly higher than that of the PCL (10.75%) and Mo-PCL (15.9%) groups ($p < 0.001$). By day 20, wounds in the SBST group were nearly fully closed with an average healing rate of 96.1%, whereas the PCL and Mo-PCL groups showed healing rates of 68.37% and 68.47%, respectively, with approximately 30% of the wound area remaining unhealed ($p < 0.001$). Notably, no statistically significant difference was observed between the PCL and Mo-PCL groups at any time point ($p > 0.05$), indicating that Mo loading alone did not markedly improve the wound-healing outcome.

Masson's trichrome staining (Figure 8D) revealed that the SBST group exhibited the longest neo-epidermis and the narrowest granulation tissue width, suggesting minimal scar formation in the newly regenerated tissue (Figures 8H and 8I). In addition, collagen deposition in the SBST group was markedly increased (Figure 8J). Doppler blood flow imaging on day 15 (Figure 8E) showed the strongest perfusion signals in the SBST group, indicating enhanced angiogenesis and local circulation, which are indicative of improved wound healing. H&E staining further confirmed more complete epithelial architecture reconstruction in the SBST-treated wounds. More prominent rete ridges were observed at the wound center in the SBST group—hallmarks of epithelial maturation that anchor the neo-epidermis to the underlying granulation tissue and help prevent secondary detachment. Moreover, the SBST group showed the lowest number of neutrophils (blue arrows) in granulation tissue, corresponding to reduced inflammation and more compact tissue organization (Figure S32). Quantitative analysis of neutrophil infiltration (Figure S33) demonstrated significantly fewer neutrophils in the SBST group compared with the PCL and blank control groups, indicating a potent anti-inflammatory effect. Sirius Red staining (Figure 8F) further revealed that the SBST group generated more newly formed collagen fibers, which were more orderly aligned and directionally organized—favorable conditions for high-quality tissue regeneration. Re-epithelialization requires active epithelial cell proliferation to replenish the cellular pool for wound repair. To elucidate the role of remodeled EFs in epithelial regeneration, immunohistochemical staining for Ki67 was performed to evaluate cell proliferation. Ki67 is a highly conserved nuclear protein widely used as a marker for cell proliferation. It is strongly expressed in actively dividing cells during the G1, S, G2, and M phases but is absent in quiescent (G0) cells, thereby serving as an indicator of cell cycle progression. An immunohistochemical analysis of Ki67 (Figure 8G) revealed markedly increased expression of Ki67-positive cells in the SBST group. By contrast, relatively lower Ki67 expression was detected in the PCL and Mo-PCL groups, suggesting that the application of a low-intensity direct current EF significantly promotes epithelial cell proliferation ($p < 0.001$; Figure 8K).

Taken together, these findings, consistent with the *in vitro* results, demonstrate that SBST not only markedly accelerates diabetic wound closure but also promotes high-quality tissue regeneration by enhancing local blood perfusion and stimulating epithelial cell proliferation. These results highlight the favorable bioactivity and promising clinical potential of SBST in diabetic wound management.

Conclusion

In this study, we developed an SBST driven by endogenous tissue fluid, capable of continuously delivering stable electrical stimulation to accelerate wound healing both *in vitro* and *in vivo*. By leveraging the self-assembly properties of MXene nanosheets to construct highly ordered nanochannels, we regulate the oxidation rate of the Mg electrode, effectively delaying its degradation, significantly extending device lifespan, and maintaining stable output. The SBST integrates Mg/Mo nanoelectrodes with a breathable and flexible electrospun PCL substrate, exhibiting excellent biocompatibility, mechanical flexibility, and antibacterial properties. Moreover, its manufacturing process is not only seamlessly compatible with existing medical textile systems but also demonstrates feasibility and stability for large-scale production, thereby laying a solid foundation for clinical translation and industrialization. This design combines energy autonomy, mechanical flexibility, and biodegradability, overcoming the critical limitations of conventional bioelectronic devices that rely on external power sources, rigid packaging, and wired connections.

Crucially, SBST demonstrates consistent structure-electric signal-functional outcome relationships across multiple tissue types: it enhances closure and epithelialization in skin wounds, promotes collagen alignment and functional recovery in tendon injuries, and accelerates closure and vascularization in diabetic wounds. These results highlight the broad applicability of SBST for acute, chronic, and mechanically demanding tissue healing scenarios, providing a versatile platform for self-powered, bioresorbable electrical stimulation therapies. By overcoming key

Figure 8. SBST accelerated and guided difficult-to-heal skin tissue self-healing in the diabetic porcine model

(A) Schematic diagram of wound care in diabetic Bama mini pigs.
(B) Images of wounds in different groups at different care times.
(C) Statistical analysis of wound area at different care times ($n = 4$).
(D) Masson staining of wounds in different experimental groups.
(E) Blood vessel density of the healing area in different experimental groups on the 15th day.
(F) Sirius Red staining in the central part of the repaired tissue in different groups (day 20).
(G) Immunohistochemical staining of Ki67 in different groups. Ki67+ cells are shown in orange.
(H) Quantitative analysis of the length of newly formed epidermis ($n = 4$).
(I) Quantitative analysis of granulation tissue width ($n = 4$).
(J) Collagen volume fraction of the healing area ($n = 4$).
(K) Semi-quantitative analysis of the density of Ki67+ cells ($n = 4$).
In (C) and (H)–(K), data are presented as mean ± SD. In (C) and (H)–(K), statistical significance was determined by the one-way ANOVA. $^{*}p < 0.05$, $^{**}p < 0.01$, $^{***}p < 0.001$, $^{****}p < 0.0001$.

Please cite this article in press as: Wang et al., Tissue-fluid-driven symbiotic electronic textile accelerates and guides tissue self-healing, Cell Biomaterials (2026), https://doi.org/10.1016/j.celbio.2026.100375

limitations of current galvanic cell systems—such as unstable output, mechanical rigidity, and limited operational lifespan—SBST offers a robust, scalable, and clinically translatable strategy for personalized and intelligent regenerative medicine.

METHODS

Materials

Ti_3AlC_2 powder was purchased from 11Technology. Lithium fluoride (LiF, AR) was purchased from Aladdin. PCL (6500) was purchased from Jinan Daigang Biomaterial. Concentrated hydrochloric acid (HCl, 36.5%), STZ, and dichloromethane (DCM; 99.8%) were purchased from Macklin. Calcein acetoxymethyl ester (Calcein-AM) and propidium iodide (PI), CCK-8, Dulbecco's modified Eagle's medium (DMEM), phosphate-buffered saline (PBS) buffer, penicillin-streptomycin solution, 4% paraformaldehyde fix solution, and sodium citrate buffer (0.1 mol/L, pH 4.5) were purchased from Solarbio. Tetramethylrhodamine isothiocyanate (TRITC) phalloidin was purchased from Abcam. Hochest 33342 was purchased from Thermo. Matrigel was purchased from Corning. Taq Pro Universal SYBR qPCR Master Mix, 4 × g DNA wiper Mix, and HiScript III qRT superMix were purchased from Vazyme. B7-2 (CD86) antibody (sc-52448) and CD206/Mannose Receptor/MMR antibody were purchased from Santa Cruz Biotechnology.

Preparation of SBST

PCL was dissolved in DCM at a concentration of 15 wt % and stirred for 6 h to obtain a homogeneous solution. Random PCL nanofiber membranes were fabricated via electrospinning using a 5 mL syringe (23G needle) at a flow rate of 1.5 mL/h, with a needle-to-collector distance of 10 cm. The collector reciprocated over a 10 cm range at a speed of 20 cm/min and rotated at 300 rpm. A voltage of +7 kV/−3 kV was applied for 120 min. For the preparation of aligned PCL fibers, the collector rotational speed was increased to 1,500 rpm, and the reciprocation speed was reduced to 3 cm/min, enabling fiber alignment along the rotational direction. All membranes were vacuum-dried overnight at room temperature (RT) to remove residual solvent. A patterned mask was fabricated on 1 mm thick acrylic using laser cutting for later metal deposition. To enhance metal adhesion, the PCL membranes underwent plasma treatment to improve surface activity and hydrophilicity. Mo and Mg were sequentially deposited via magnetron sputtering (Denton, Discovery 635, USA). Mo was sputtered at 100 W for 60 min, and Mg was deposited in 10 cycles (45 min sputtering, 15 min cooling, 120 W) to prevent substrate overheating. Finally, a 20 mg/mL MXene solution (prepared by the method previously reported[33]) was sprayed onto the Mg layer using an airbrush. By adjusting air pressure, spray rate, and distance, multilayer coatings were formed and dried at RT, yielding conductive MXene-coated electronic textiles.

Characterization measurements

The microstructure and elemental composition of the nanofibers were characterized using a Nova 450 SEM equipped with a Raith/EDAX/EDS system. The voltage and current of the electronic textiles were measured using an electrometer (Keithley 6517B) and an oscilloscope (LeCroy, HDO6104). The stress-strain curves were obtained using an ESM301/Mark-10 system. The I-V curves were recorded using a semiconductor parameter analyzer (Keithley 4200), and the Tafel curves were measured using an electrochemical workstation (CHI660E). The i-t curves were recorded using an electrometer and an oscilloscope.

Cell biocompatibility and proliferation evaluations

L929 cells were cultured with standard DMEM (Gibco) supplemented with 1% penicillin/streptomycin (Gibco) and 10% fetal bovine serum (FBS, Gibco) at 37°C in a 5% CO_2 atmosphere, and the medium was replaced every 2 days. Firstly, the biocompatibility of the materials was tested by a live/dead assay (Solarbio, China). Samples of different materials weighing 10 mg were first soaked in 20 mL of DMEM for 24 h, and the leachate was retained. Cells were incubated in the leachate for 3 days and then stained with a live/dead assay according to the reagent vendor's instructions. Briefly, the cell samples were incubated with the prepared solution at 37°C for 20 min and then observed using a fluorescence microscope (DMI 6000). Further, cell proliferation level for 1, 2, and 3 days was evaluated by a CCK-8 (Solarbio, China) assay. Specifically, following the removal of the medium and the washing of the cell samples with PBS solution, the samples were incubated with medium containing 10% CCK-8 reagent. After incubation at 37°C for 1.5 h, absorbance at 450 nm was measured using a microplate reader (Thermo Fisher Scientific, USA).

Antibacterial ability

The antibacterial activity of the electronic textiles was evaluated using Gram-positive bacteria (*S. aureus* 29213) and Gram-negative bacteria (*E. coli* ATCC 25922). Briefly, bacteria were cultured to a concentration of 2–3 × 10^9 colony-forming units (CFUs)/mL and then diluted to 2–3 × 10^4 CFU/mL for antibacterial testing. Sterilized PCL and SBST samples (1 cm in diameter) were immersed in 1 mL of bacterial suspension and incubated at 37°C for 6 h. Afterward, the bacterial suspensions were diluted and spread on agar plates for colony counting to assess antibacterial performance. For morphological observation, the bacteria-attached samples were fixed in 2.5% glutaraldehyde overnight, dehydrated in a graded ethanol series (50%, 60%, 70%, 80%, 90%, and 100%) for 30 min each, dried, and observed by SEM. Additionally, PCL and SBST samples were immersed in 1 mL of crystal violet solution (50 μM). At intervals of 0.5 h, the solutions were photographed, and the absorbance was measured using a ultraviolet-visible (UV-vis) spectrophotometer to monitor dye degradation. Using a sterile biopsy puncher, a full-thickness skin lesion of 1 cm in size was made on the back of the mice. Then, 50 μL of *S. aureus* with a concentration of 10^6 CFU/mL was dripped onto the wound to induce infection. The mice were randomly divided into two groups, namely PCL and SBST treatment. 1 day later, the wound surface was gently swabbed with sterile cotton swabs to collect exudates and bacteria, and smears were then prepared for bacterial colony counting by plating on agar plates.

Cell biocompatibility

Before cell experiments, PCL and SBST patches were cut into 1 cm diameter discs, sterilized by UV irradiation and immersion in 75% ethanol, rinsed three times with PBS, and placed into 24-well plates. To prevent floating, Polydimethylsiloxane (PDMS) rings (7 mm inner diameter) were used to fix the patches.

Please cite this article in press as: Wang et al., Tissue-fluid-driven symbiotic electronic textile accelerates and guides tissue self-healing, Cell Biomaterials (2026), https://doi.org/10.1016/j.celbio.2026.100375

Cells cultured on coverslips were used as controls. HUVECs were seeded at a density of 8×10^3 cells/well for subsequent assays. Cell proliferation was evaluated using a CCK-8 (Dojindo). After incubation with culture medium containing 10% CCK-8 reagent for 1 h, 100 μL of the supernatant was transferred to a 96-well plate, and the absorbance at 450 nm was recorded using a microplate reader. Live/dead staining was performed using Calcein-AM and PI. After trypsinization and centrifugation, cells were incubated with Calcein-AM at 37°C for 25 min, followed by PI staining at RT for 5 min. After washing with PBS, cells were resuspended, dropped onto slides, and observed using a confocal laser scanning microscope. Live and dead cells were indicated by green and red fluorescence, respectively. For cytoskeleton staining, cells were fixed with 4% paraformaldehyde for 10 min, rinsed with PBS, and incubated with rhodamine-phalloidin (Abcam, 1:1,000) at 37°C for 1 h. After washing, nuclei were stained with Hoechst 33342 (Thermo, 1:1,000) for 10 min. Samples were imaged using a confocal laser scanning microscope. Samples were washed with PBS and imaged using a confocal laser scanning microscope.

Hemolytic test

To prepare the extract solutions, PCL and SBST membranes (6 cm^2/mL) were soaked in PBS at 37°C for 24 h. Deionized water and PBS served as positive and negative controls, respectively. Fresh rat blood was diluted 10-fold with PBS, and 100 μL of the diluted blood was added to 1 mL of each sample. After incubation at 37°C for 60 min, samples were centrifuged at 1,000 *g* for 5 min. The absorbance of the supernatant was measured at 545 nm using a microplate reader.

Cell migration assay and angiogenesis assay

For the cell migration assay, 1×10^5 human epidermal keratinocyte cell line (HaCaT) cells were seeded in 24-well plates. After 24 h of incubation to form a cell monolayer, a scratch was created using a 100 μL pipette tip. The medium was replaced with serum-free high-glucose DMEM, and cells were divided into three groups: Ctrl (no treatment), PCL-Mo, and SBST. Cell migration was recorded at 0, 3, and 6 h. For the tube formation assay, Matrigel was thawed at 4°C and coated (20 μL/well) in pre-chilled 24-well plates. After overnight incubation at 4°C and 45 min at 37°C for gelation, HUVECs were seeded. PCL-Mo and SBST membranes were added to PBS. Images were taken every 2 h and analyzed by ImageJ to quantify node numbers, total branch length, and average branch length.

In vivo electrical testing

In this study, electrometers, oscilloscopes, and platinum electrodes were used to measure and analyze the potential and current in the wound area. In the experiment, the positive and negative electrodes of the electrometer were connected to two platinum electrodes separated by 1 mm, and their potential difference on the wound was recorded to characterize the average EF strength in the area.

Full-thickness mouse skin wound model

All procedures were approved by the Animal Ethics Committee of the Beijing Institute of Nanoenergy and Nanosystems (2022008LZ). In this study, 24 male Kunming mice (6 weeks old) were purchased from Beijing Vital River Laboratory Animal Technology. All mice were housed in a specific pathogen-free (SPF) facility for 1 week for acclimation, with free access to food and water under standard conditions (23°C–26°C, 40%–60% humidity, 12 h light/dark cycle). Mice were anesthetized with 1%–3% isoflurane, and the dorsal hair was removed. A 1 cm full-thickness skin wound was created on the back using a sterile biopsy punch. The mice were randomly divided into four groups ($n = 6$ per group): Ctrl, PCL, SBST-M (Mg electrode in the center), and SBST-S (Mg electrode in the outer ring). The wounds were covered with Tegaderm to prevent contraction. Wound healing was monitored every 3 days, and the wound area was photographed and analyzed using ImageJ to calculate the healing rate. Histological analyses of the wounds were performed on days 9 and 21. Three mice from each group were euthanized, and wound tissues were harvested and fixed in formalin. The samples were embedded in paraffin, sectioned, and subjected to H&E staining to evaluate the wound-healing process. Masson's trichrome staining and Sirius Red staining were also conducted to assess collagen deposition. In addition, immunofluorescence staining for CD31 and vascular endothelial growth factor A (VEGFA), as well as CD86 and CD206, was performed to evaluate angiogenesis and tissue inflammation.

In vivo degradation and safety assessment

SBST was sterilized using ultraviolet irradiation and 75% ethanol for 1 h before being subcutaneously implanted into the dorsal region of Kunming mice. On day 15, the implantation site was re-exposed to observe the degradation status of SBST, and images were captured using a Nikon D780 camera. The mice were then euthanized, and blood samples were collected for biochemical and hematological analyses.

Rat Achilles tendon rupture model

All procedures were approved by the Animal Ethics Committee of the Beijing Institute of Nanoenergy and Nanosystems (2022008LZ). Nine male SD rats (200 g) were fasted for 8 h before surgery with free access to water. After weighing, rats were anesthetized with isoflurane and fixed in a prone position. The hair on the right hind limb was removed and disinfected. A longitudinal skin incision was made to expose the Achilles tendon, which was then transected and sutured using a modified Kessler technique with 6-0 sutures.

Rats were randomly divided into three groups ($n = 3$ per group): Ctrl (suture only), PCL (sutured tendon wrapped with PCL patch), and SBST (sutured tendon wrapped with SBST patch for electrical stimulation). The incision was closed and disinfected, followed by routine care. Body weight was recorded regularly. The footprint of each rat was collected at 1, 2, 3, and 4 weeks post-surgery, and the sciatic functional index (SFI) was used to evaluate tendon function. After euthanasia by overdose anesthesia, the Achilles tendons were photographed and collected for H&E and Masson staining for histological analysis.

Full-thickness diabetic porcine wound model

All procedures were performed by qualified veterinary surgeons under sterile conditions with ethical approval (NNXMJS001-20241112P4-1P-SY). Bama minipig (18–22 kg)

Cell Biomaterials
Article

CellPress
OPEN ACCESS

was used in this study. The porcine model was established by Nongnong Biotechnology (Beijing, China). After 16 h fasting, the porcine was anesthetized, weighed, and an ear vein catheter was established. STZ was dissolved in 0.1 M citrate buffer (pH 4.2–4.5), filtered through a 0.22 μm filter, and intravenously injected at a dose of 85 mg/kg. Porcine with fasting blood glucose levels > 11.1 mmol/L for 2 consecutive days were considered diabetic. Blood glucose was monitored daily, and insulin (12–20 U) was administered when glucose exceeded 20 mmol/L. Diabetic porcine was anesthetized with a mixture of Zoletil 100 and xylazine. The dorsal hair was removed, and six full-thickness circular wounds (1.5 cm diameter) were created on both sides of the spine. Wounds were divided into three groups based on wound dressing: PCL, Mo-PCL, and SBST. Dressings were changed every 3 days, and wound healing was monitored by photographing and measuring the wound area. Body weight and blood glucose were recorded regularly. On day 15, blood perfusion in regenerated skin was assessed using a Doppler imaging system (MoorFLPI-2, UK). On day 20, pigs were euthanized, and wound tissues were collected for H&E, Masson's trichrome, and Sirius Red staining to evaluate tissue structure and collagen deposition.

Transcriptome sequencing and data analysis

Wound tissues were collected on day 6 post-injury for RNA extraction using TRIzol reagent. RNA quality was assessed with a 5300 Bioanalyzer, and concentration was measured using a NanoDrop ND-2000. RNA purification, reverse transcription, library preparation, and sequencing were performed by Majorbio (Shanghai, China) following the manufacturer's protocols. Sequencing was conducted on the NovaSeq X Plus platform (PE150, Illumina). Differential gene expression analysis was performed using DESeq2, with $|\log2FC| \geq 1$ and false discovery rate (FDR) < 0.05 considered significant. GO enrichment and KEGG pathway analyses were conducted using Goatools and Python scipy packages.

qPCR experiments

Total RNA extracted from wound tissues was quantified and assessed for purity using a NanoDrop spectrophotometer. RNA was then reverse-transcribed into cDNA using a commercial kit. qPCR reactions were prepared with cDNA templates, specific primers, SYBR dye, and reaction buffer and performed using a thermal cycler. Relative gene expression was calculated using the Cycle Threshold **Cycle Threshold ((**Ct) method with β-actin as the reference gene. Primer sequences are listed in Table S6.

Statistical analysis

Statistical analyses were performed with the Origin software program, Prism 8.0 software (GraphPad software), and ImageJ software, and the results were reported as the mean ± SD. Analysis of significance difference was calculated by using one-way ANOVA and unpaired Student's *t* test. Statistical differences were shown with four significance levels ($^{*}p < 0.05$, $^{**}p < 0.01$, $^{***}p < 0.001$, $^{****}p < 0.0001$).

RESOURCE AVAILABILITY

Lead contact

Further information and requests for resources should be directed to and will be fulfilled by the lead contact, Han Ouyang (ouyanghan@ucas.ac.cn).

Materials availability

This study did not generate any new, unique reagents.

Data and code availability

This study did not generate any datasets.

ACKNOWLEDGMENTS

Funding: the National Natural Science Foundation of China grants 52373256 (to H.O.), T2125003 (to Z.L.), and U25A20417 (to Z.L.); the Youth Innovation Promotion Association CAS grant 2023176 (to H.O.); the Beijing Natural Science Foundation grants 7232347 (to H.O.), 7264408 (to E.W.), L245015 (to Z.L.), Z240022 (to Z.L.), and 25JL006 (to Z.L.); the Beijing Nova Program grant 2024047 (to H.O.); and the Fundamental Research Funds for the Central Universities grant.

The authors thank the members of the University of Chinese Academy of Sciences research facilities for their help in microfabrication/characterization, as well as the staff of the Beijing Institute of Nanoenergy and Nanosystems Biological Laboratory Center for their assistance in biological experiments.

AUTHOR CONTRIBUTIONS

H.O., Z.L., J.Z., and L.X. conceived and coordinated the project and experiments. E.W., L.X., D.J., and B.S. assisted in concept development, sample preparation, and manuscript writing. E.W., L.L., C.Z., and Y.Q. conducted the material preparation and characterization. E.W. and J.X. conducted the electrochemical testing. J.H., X.C., and L.X. conducted the cell experiment. E.W., L.X., and Y.R. conducted the *in vivo* animal experiments (SD rats). H.F., E.W., and L.X. conducted the *in vivo* animal experiments (pig). E.W., L.L., and C.Z. conducted the *in vivo* animal experiments. E.W. and L.L. processed the data and drew the figures. E.W., L.X., and H.O. wrote the paper. H.O., Z.L., J.Z., and L.X. directed the project. All authors read and revised the manuscript.

DECLARATION OF INTERESTS

The authors declare no competing interests.

SUPPLEMENTAL INFORMATION

Supplemental information can be found online at https://doi.org/10.1016/j.celbio.2026.100375.

Received: October 14, 2025
Revised: December 21, 2025
Accepted: January 26, 2026

REFERENCES

1. Wang, C., Shirzaei Sani, E., Shih, C.-D., Lim, C.T., Wang, J., Armstrong, D.G., and Gao, W. (2024). Wound management materials and technologies from bench to bedside and beyond. Nat. Rev. Mater. *9*, 550–566. https://doi.org/10.1038/s41578-024-00693-y.
2. Huang, Y., Yao, K., Zhang, Q., Huang, X., Chen, Z., Zhou, Y., and Yu, X. (2024). Bioelectronics for electrical stimulation: materials, devices and biomedical applications. Chem. Soc. Rev. *53*, 8632–8712. https://doi.org/10.1039/D4CS00413B.
3. Xiao, A., Jiang, X., Hu, Y., Li, H., Jiao, Y., Yin, D., Wang, Y., Sun, H., Wu, H., Lin, L., et al. (2024). A degradable bioelectronic scaffold for localized cell

transfection toward enhancing wound healing in a 3D Space. Adv. Mater. *36*, e2404534. https://doi.org/10.1002/adma.202404534.

4. Shi, J., Lin, Y., Li, P., Mickel, P., Sun, C., Parekh, K., Ma, J., Kim, S., Ashwood, B., Meng, L., et al. (2024). Monolithic-to-focal evolving biointerfaces in tissue regeneration and bioelectronics. Nat. Chem. Eng. *1*, 73–86. https://doi.org/10.1038/s44286-023-00008-y.
5. Theocharidis, G., Yuk, H., Roh, H., Wang, L., Mezghani, I., Wu, J., Kafanas, A., Contreras, M., Sumpio, B., Li, Z., et al. (2022). A strain-programmed patch for the healing of diabetic wounds. Nat. Biomed. Eng. *6*, 1118–1133. https://doi.org/10.1038/s41551-022-00905-2.
6. Tören, E., and Mazari, A.A. (2024). Pullulan/collagen scaffolds promote chronic wound healing via mesenchymal stem cells. Micro *4*, 599–620. https://doi.org/10.3390/micro4040037.
7. Shirzaei Sani, E., Xu, C., Wang, C., Song, Y., Min, J., Tu, J., Solomon, S.A., Li, J., Banks, J.L., Armstrong, D.G., et al. (2023). A stretchable wireless wearable bioelectronic system for multiplexed monitoring and combination treatment of infected chronic wounds. Sci. Adv. *9*, eadf7388. https://doi.org/10.1126/sciadv.adf7388.
8. Kaveti, R., Jakus, M.A., Chen, H., Jain, B., Kennedy, D.G., Caso, E.A., Mishra, N., Sharma, N., Uzunoğlu, B.E., Han, W.B., et al. (2024). Water-powered, electronics-free dressings that electrically stimulate wounds for rapid wound closure. Sci. Adv. *10*, eado7538. https://doi.org/10.1126/sciadv.ado7538.
9. Wang, L., Lu, C., Yang, S., Sun, P., Wang, Y., Guan, Y., Liu, S., Cheng, D., Meng, H., Wang, Q., et al. (2020). A fully biodegradable and self-electrified device for neuroregenerative medicine. Sci. Adv. *6*, eabc6686. https://doi.org/10.1126/sciadv.abc6686.
10. Koo, J., MacEwan, M.R., Kang, S.-K., Won, S.M., Stephen, M., Gamble, P., Xie, Z., Yan, Y., Chen, Y.-Y., Shin, J., et al. (2018). Wireless bioresorbable electronic system enables sustained nonpharmacological neuroregenerative therapy. Nat. Med. *24*, 1830–1836. https://doi.org/10.1038/s41591-018-0196-2.
11. Wu, H., Wang, Y., Li, H., Hu, Y., Liu, Y., Jiang, X., Sun, H., Liu, F., Xiao, A., Chang, T., et al. (2024). Accelerated intestinal wound healing via dual electrostimulation from a soft and biodegradable electronic bandage. Nat. Electron. *7*, 299–312. https://doi.org/10.1038/s41928-024-01138-8.
12. Liu, Y., Dzidotor, G., Le, T.T., Vinikoor, T., Morgan, K., Curry, E.J., Das, R., McClinton, A., Eisenberg, E., Apuzzo, L.N., et al. (2022). Exercise-induced piezoelectric stimulation for cartilage regeneration in rabbits. Sci. Transl. Med. *14*, eabi7282. https://doi.org/10.1126/scitranslmed.abi7282.
13. Shan, Y., Xu, L., Cui, X., Zhang, J., Ouyang, H., Wang, X., Huang, J., Xue, J., Wang, K., Wang, D., et al. (2025). A neurodevelopment-inspired self-evolving scaffold for nerve regeneration. Cell Biomater. *1*, 100006. https://doi.org/10.1016/j.celbio.2024.100006.
14. Cui, X., Xu, L., Shan, Y., Li, J., Ji, J., Wang, E., Zhang, B., Wen, X., Bai, Y., Luo, D., et al. (2024). Piezocatalytically-induced controllable mineralization scaffold with bone-like microenvironment to achieve endogenous bone regeneration. Sci. Bull. *69*, 1895–1908. https://doi.org/10.1016/j.scib.2024.04.002.
15. Wang, T., Ouyang, H., Luo, Y., Xue, J., Wang, E., Zhang, L., Zhou, Z., Liu, Z., Li, X., Tan, S., et al. (2024). Rehabilitation exercise–driven symbiotic electrical stimulation system accelerating bone regeneration. Sci. Adv. *10*, eadi6799. https://doi.org/10.1126/sciadv.adi6799.
16. Vinikoor, T., Dzidotor, G.K., Le, T.T., Liu, Y., Kan, H.-M., Barui, S., Chorsi, M.T., Curry, E.J., Reinhardt, E., Wang, H., et al. (2023). Injectable and biodegradable piezoelectric hydrogel for osteoarthritis treatment. Nat. Commun. *14*, 6257. https://doi.org/10.1038/s41467-023-41594-y.
17. Zhang, X., Wang, Z., Jiang, H., Zeng, H., An, N., Liu, B., Sun, L., and Fan, Z. (2023). Self-powered enzyme-linked microneedle patch for scar-prevention healing of diabetic wounds. Sci. Adv. *9*, eadh1415. https://doi.org/10.1126/sciadv.adh1415.
18. Xue, H., Jin, J., Tan, Z., Chen, K., Lu, G., Zeng, Y., Hu, X., Peng, X., Jiang, L., and Wu, J. (2024). Flexible, biodegradable ultrasonic wireless electrotherapy device based on highly self-aligned piezoelectric biofilms. Sci. Adv. *10*, eadn0260. https://doi.org/10.1126/sciadv.adn0260.
19. Xiang, L., Liang, J., Wang, Z., Lin, F., Zhuang, Y., Saiding, Q., Wang, F., Deng, L., and Cui, W. (2023). Motion lubrication suppressed mechanical activation via hydrated fibrous gene patch for tendon healing. Sci. Adv. *9*, eadc9375. https://doi.org/10.1126/sciadv.adc9375.
20. Zhang, Y., Lee, G., Li, S., Hu, Z., Zhao, K., and Rogers, J.A. (2023). Advances in bioresorbable materials and electronics. Chem. Rev. *123*, 11722–11773. https://doi.org/10.1021/acs.chemrev.3c00408.
21. Yao, G., Kang, L., Li, C., Chen, S., Wang, Q., Yang, J., Long, Y., Li, J., Zhao, K., Xu, W., et al. (2021). A self-powered implantable and bioresorbable electrostimulation device for biofeedback bone fracture healing. Proc. Natl. Acad. Sci. USA *118*, e2100772118. https://doi.org/10.1073/pnas.2100772118.
22. Luo, R., Dai, J., Zhang, J., and Li, Z. (2021). Accelerated skin wound healing by electrical stimulation. Adv. Healthc. Mater. *10*, e2100557. https://doi.org/10.1002/adhm.202100557.
23. Jiang, Y., Trotsyuk, A.A., Niu, S., Henn, D., Chen, K., Shih, C.-C., Larson, M.R., Mermin-Bunnell, A.M., Mittal, S., Lai, J.-C., et al. (2023). Wireless, closed-loop, smart bandage with integrated sensors and stimulators for advanced wound care and accelerated healing. Nat. Biotechnol. *41*, 652–662. https://doi.org/10.1038/s41587-022-01528-3.
24. Zhao, C., Park, J., Root, S.E., and Bao, Z. (2024). Skin-inspired soft bioelectronic materials, devices and systems. Nat. Rev. Bioeng. *2*, 671–690. https://doi.org/10.1038/s44222-024-00194-1.
25. Li, J., Xu, Y., and Gao, W. (2024). Injectable and retrievable soft electronics. Nat. Mater. *23*, 591–593. https://doi.org/10.1038/s41563-024-01877-1.
26. Shi, J., Kim, S., Li, P., Dong, F., Yang, C., Nam, B., Han, C., Eig, E., Shi, L.L., Niu, S., et al. (2024). Active biointegrated living electronics for managing inflammation. Science *384*, 1023–1030. https://doi.org/10.1126/science.adl1102.
27. Lee, D.-M., Kang, M., Hyun, I., Park, B.-J., Kim, H.J., Nam, S.H., Yoon, H.-J., Ryu, H., Park, H.-M., Choi, B.-O., and Kim, S.-W. (2023). An on-demand bioresorbable neurostimulator. Nat. Commun. *14*, 7315. https://doi.org/10.1038/s41467-023-42791-5.
28. Xu, L., Wang, E., Kang, Y., Fu, D., Luo, L., Quan, Y., Xi, Y., Huang, J., Cui, X., Zeng, J., et al. (2025). Schottky nanodiodes array enabled triboelectric nanosecond pulse generator for ultralow-cost tumor therapy. Device *3*, 100721. https://doi.org/10.1016/j.device.2025.100721.
29. Choi, Y.S., Yin, R.T., Pfenniger, A., Koo, J., Avila, R., Benjamin Lee, K., Chen, S.W., Lee, G., Li, G., Qiao, Y., et al. (2021). Fully implantable and bioresorbable cardiac pacemakers without leads or batteries. Nat. Biotechnol. *39*, 1228–1238. https://doi.org/10.1038/s41587-021-00948-x.
30. Choi, Y.S., Jeong, H., Yin, R.T., Avila, R., Pfenniger, A., Yoo, J., Lee, J.Y., Tzavelis, A., Lee, Y.J., Chen, S.W., et al. (2022). A transient, closed-loop network of wireless, body-integrated devices for autonomous electrotherapy. Science *376*, 1006–1012. https://doi.org/10.1126/science.abm1703.
31. Li, S., Lu, D., Li, S., Liu, J., Xu, Y., Yan, Y., Rodriguez, J.Z., Bai, H., Avila, R., Kang, S., et al. (2024). Bioresorbable, wireless, passive sensors for continuous pH measurements and early detection of gastric leakage. Sci. Adv. *10*, eadj0268. https://doi.org/10.1126/sciadv.adj0268.
32. Ouyang, H., Liu, Z., Li, N., Shi, B., Zou, Y., Xie, F., Ma, Y., Li, Z., Li, H., Zheng, Q., et al. (2019). Symbiotic cardiac pacemaker. Nat. Commun. *10*, 1821. https://doi.org/10.1038/s41467-019-09851-1.
33. Wang, E., Wu, M., Luo, L., Cui, X., Xu, L., Luo, R., Zou, Y., Le, T., Shan, Y., Quan, Y., et al. (2025). Symbiotic biodegradable flexible supercapacitor in vivo. Device *3*, 100724. https://doi.org/10.1016/j.device.2025.100724.
34. Sheng, H., Zhou, J., Li, B., He, Y., Zhang, X., Liang, J., Zhou, J., Su, Q., Xie, E., Lan, W., et al. (2021). A thin, deformable, high-performance supercapacitor implant that can be biodegraded and bioabsorbed within

Please cite this article in press as: Wang et al., Tissue-fluid-driven symbiotic electronic textile accelerates and guides tissue self-healing, Cell Biomaterials (2026), https://doi.org/10.1016/j.celbio.2026.100375

an animal body. Sci. Adv. *7*, eabe3097. https://doi.org/10.1126/sciadv.abe3097.

35. Li, P., Zhang, J., Hayashi, H., Yue, J., Li, W., Yang, C., Sun, C., Shi, J., Huberman-Shlaes, J., Hibino, N., and Tian, B. (2024). Monolithic silicon for high spatiotemporal translational photostimulation. Nature *626*, 990–998. https://doi.org/10.1038/s41586-024-07016-9.
36. Ghosh, S.K., Matino, F., Favrin, F.L., Tonazzini, I., D'Orsi, R., de la Ossa, J.G., Camposeo, A., Li, J., Liu, W., Hacker, T.A., et al. (2025). Fully biodegradable hierarchically designed high-performance nanocellulose piezo-arrays. Sci. Adv. *11*, eads0778. https://doi.org/10.1126/sciadv.ads0778.
37. Bai, Y., Meng, H., Li, Z., and Wang, Z.L. (2024). Degradable piezoelectric biomaterials for medical applications. MedMat *1*, 40–49. https://doi.org/10.1097/mm9.0000000000000002.
38. Ma, X., Zhou, Y., Xin, M., Yuan, H., Chao, D., Liu, F., Jia, X., Sun, P., Wang, C., Lu, G., et al. (2024). A Mg battery-integrated bioelectronic patch provides efficient electrochemical stimulations for wound healing. Adv. Mater. *36*, e2410205. https://doi.org/10.1002/adma.202410205.
39. Xin, J., Gao, L., Zhang, W., Song, X., Yang, Y., Li, W., Zhou, X., Zhang, H., Wang, Z., Wang, Z., et al. (2025). A thermogalvanic cell dressing for smart wound monitoring and accelerated healing. Nat. Biomed. Eng. *10*, 80–93. https://doi.org/10.1038/s41551-025-01440-6.
40. Liu, J., Cheng, H., Yuan, X., Wang, L., and Gao, J. (2024). Amphipathic medical composite cotton gauze with unidirectional drainage and anti-adhesion properties for wound healing. Cellulose *31*, 7613–7627. https://doi.org/10.1007/s10570-024-06063-9.
41. Libanori, A., Chen, G., Zhao, X., Zhou, Y., and Chen, J. (2022). Smart textiles for personalized healthcare. Nat. Electron. *5*, 142–156. https://doi.org/10.1038/s41928-022-00723-z.
42. Wu, H., Xiao, G., He, X., Ju, J., Zhang, J., Sathishkumar, G., Yu, L., Zhang, K., Rao, X., Lu, Z., et al. (2024). A wound exudate-activated yarn battery for antimicrobial electrical fabric dressing. Adv. Funct. Mater. *34*, 2405114. https://doi.org/10.1002/adfm.202405114.
43. Sun, Z., Jin, Y., Luo, J., Li, L., Ding, Y., Luo, Y., Qi, Y., Li, Y., Zhang, Q., Li, K., et al. (2024). A bioabsorbable mechanoelectric fiber as electrical stimulation suture. Nat. Commun. *15*, 8462. https://doi.org/10.1038/s41467-024-52354-x.
44. Zhu, Y., Zhang, C., Liang, Y., Shi, J., Yu, Q., Liu, S., Yu, D., and Liu, H. (2024). Advanced postoperative tissue antiadhesive membranes enabled with electrospun nanofibers. Biomater. Sci. *12*, 1643–1661. https://doi.org/10.1039/D3BM02038J.
45. Yang, L., Wang, P., Zhang, Y., Zhou, J., Bi, X., Qian, Z., Hou, S., Li, L., and Fan, Y. (2025). Hybrid cell membrane coating orchestrates foreign-body reactions, anti-adhesion, and pro-regeneration in abdominal wall reconstruction. Biomaterials *321*, 123289. https://doi.org/10.1016/j.biomaterials.2025.123289.